Available online at www.CivileJournal.org

Civil Engineering Journal

(E-ISSN: 2476-3055; ISSN: 2676-6957)

Vol. 12, No. 06, June, 2026

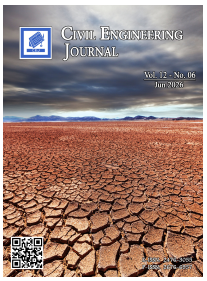

Steel-Concrete Bond Behavior Through Push-In Tests and Nonlinear Finite Element Simulations

Gehan Aouf [1*], Fouadi AlZaatiti [1, 2], Abdelrahim Sabsabi [1], Rashad Aouf [3], Mohamad Ezzedine El Dandachy [1*]

[1] *Faculty of Engineering, Beirut Arab University, Beirut 1105, Lebanon.*

[2] *Faculty of Architecture and Design, City University, Tripoli 1300, Lebanon.*

[3] *Faculty of Economics and Business Administration, Lebanese University, Tripoli 1300, Lebanon.*

Received 25 February 2026; Revised 11 May 2026; Accepted 15 May 2026; Published 01 June 2026

Abstract

This study addresses the critical need for an improved understanding of steel-concrete bond behavior under compressive stress, a condition prevalent in structural joints but under-represented by standard pull-out tests. The primary objective is to investigate the failure mechanisms of reinforced concrete specimens under quasi-static shear loading through a dual experimental and numerical approach. Experimentally, three reinforced concrete specimens were tested to provide a robust basis for numerical calibration. Subsequently, an extensive nonlinear 2D finite element analysis (FEA) using the Concrete Damaged Plasticity (CDP) framework was conducted to systematically evaluate the sensitivity of bond behavior to parameters such as concrete strength, dilation, and embedment length. The calibrated model demonstrates high reliability in predicting push-in responses. Findings reveal a critical transition in failure mechanisms, from ductile interfacial slip in shorter embedment lengths to brittle splitting failure in longer ones. Furthermore, while increased concrete strength and dilation angles enhance ultimate load capacity, shorter embedment lengths ensure more uniform stress distribution and superior bond efficiency. The novelty of this research lies in demonstrating that push-in testing offers a more representative evaluation of steel–concrete interaction than traditional methods, providing essential insights for the safer design of complex structural connections and high-density reinforcement zones.

Keywords: Steel-Concrete Interface; Bond Behavior; Push-In Test; Finite Element Modeling; Concrete Damaged Plasticity.

1. Introduction

Reinforced concrete (RC) remains the cornerstone of modern infrastructure, relying on the synergistic interaction between concrete's compressive strength and the tensile capacity of steel reinforcement. The structural integrity of these composites depends fundamentally on the bond behavior, which facilitates efficient stress transfer and ensures the monolithic performance of structural elements [1]. While this interaction is vital for serviceability, it becomes particularly critical under extreme loading, where the bond-slip mechanism dictates the overall ductility and energy dissipation of the system [2, 3]. However, the long-term durability of these structures is often compromised by the development of micro-cracks, which serve as pathways for aggressive substances that can accelerate reinforcement corrosion [4].

* Corresponding author: jihane_aouf@hotmail.com; m.dandachy@bau.edu.lb

https://doi.org/10.28991/CEJ-2026-012-06-024

Consequently, bond failure remains a primary concern, as it can significantly reduce load-bearing capacity and shorten the overall lifespan of RC infrastructure. The mechanical behavior of the bond is governed by complex parameters such as concrete strength, cover thickness, and reinforcement geometry [5]. Historically, research has utilized pull-out tests to quantify bond strength [6, 7]. While these are prevalent for evaluating interface behavior [8-10], they primarily isolate the bond under tensile forces, which may not fully represent the multiaxial stress states encountered in real-world applications [11-13].

In addition to traditional bond mechanics, recent advancements have focused on optimizing interface performance through innovative material compositions. Studies have emphasized the role of refined Interfacial Transition Zones (ITZ) in high-performance composites, demonstrating that bond degradation is significantly influenced by micro-structural density and local confinement [14, 15]. Furthermore, contemporary numerical approaches have moved beyond simplified bond-slip laws toward robust, damage-based frameworks. Recent studies have employed multi-scale Finite Element Analysis (FEA) to simulate steel–concrete interface degradation under coupled thermo-mechanical loading conditions [16, 17]. Recent advancements have expanded mesoscale and multi-scale numerical approaches for concrete damage assessment, including CT-informed modeling techniques and detailed descriptions of ITZ damage evolution [18, 19]. Such high-fidelity approaches provide greater accuracy in predicting the failure mechanisms and the onset of brittle splitting compared to traditional methodologies.

Although pull-out testing remains the most widely adopted method for bond characterization, relatively limited research has investigated push-in testing under compressive stress states. In particular, the combined effects of embedment length and concrete strength on the transition between interfacial slip and splitting failure have not been comprehensively examined. Unlike traditional pull-out tests, which focus on tensile bond behavior, the push-in test generates compressive stresses at the steel–concrete interface. This configuration provides a more representative evaluation of the multiaxial stress conditions encountered in critical structural regions, such as the anchorage zones of post-tensioned concrete elements, where high-intensity forces are transferred via a compressive path, and seismic-resistant beam-column joints, where internal force flow creates regions of high localized compression [20, 21]. These tests are also essential for characterizing the bond behavior of confined structural joints where compressive stress states dominate [14, 22, 23].

Beyond conventional reinforced concrete, accurate bond characterization is critical for emerging repair and sustainable materials. In these applications, the altered microstructure of the Interfacial Transition Zone directly dictates the load-transfer efficiency, making the investigation of bond-slip mechanisms (specifically under the compressive states of push-in testing) a prerequisite for assessing their long-term structural reliability [24, 25]. Furthermore, bond behavior has been shown to be sensitive to material composition and environmental exposure, including elevated temperatures and freeze–thaw cycles [26–28].

To capture these complex variables—ranging from material composition to environmental-induced degradation—numerical modeling has become indispensable. Finite Element Analysis (FEA) has provided profound insights into bond mechanics through the application of plasticity and damage theories [29-31]. While early research focused on classical damage mechanics [32-34], contemporary models for concrete failure have evolved toward sophisticated damage-plasticity frameworks [35]. Traditional approaches have effectively simulated bond-slip under tensile loading [36, 37] and explored advanced techniques like cohesive zone modeling [38, 39]. However, this study employs the Concrete Damaged Plasticity (CDP) model, which is uniquely suited for capturing the coupled effects of mechanical damage and the resulting degradation of the steel-concrete interface [40]. Accurate representation of interface degradation is essential for predicting stress redistribution, bond deterioration, and the associated transfer properties that influence long-term durability [41–43]. This is essential for predicting whether an interface will maintain structural integrity or undergo brittle splitting failure [44]. The CDP framework is particularly advantageous because it can simultaneously represent concrete cracking, crushing, stiffness degradation, and irreversible plastic deformation. Current numerical applications have expanded to include complex joints, such as wall-beam-slab connections under cyclic loading [45].

This study addresses the identified gap by combining experimental push-in testing with nonlinear FEA using the CDP model within ABAQUS [46-48]. The proposed framework evaluates steel–concrete bond behavior under compressive loading while accounting for key parameters such as embedment length, dilation angle, and material nonlinearity [49-51]. Particular attention is given to the transition between ductile interfacial slip and brittle splitting failure, a mechanism that remains insufficiently explored in existing literature, to provide a comprehensive validation against experimental results [52].

The main contributions of this study can be summarized as follows: (i) application of push-in testing as a reliable method to characterize steel–concrete bond behavior under compressive stress states; (ii) identification of a critical embedment length governing the transition between ductile slip and brittle splitting failure modes; (iii) development and calibration of a nonlinear Finite Element model based on the Concrete Damaged Plasticity (CDP) framework validated against experimental results; and (iv) detailed analysis of stress redistribution mechanisms, including radial and axial stresses, controlling bond degradation. These contributions provide novel insights into bond

mechanics under compressive loading conditions and address key limitations of existing pull-out-based studies, thereby advancing both numerical modeling approaches and practical design considerations for reinforced concrete structures. The findings of this study have direct implications for the design of anchorage systems, beam-column joints, and confined concrete elements, particularly in seismic regions where bond performance and ductility are critical for structural safety.

2. Experimental Program

2.1. Test Specimen Configuration

The experimental study conducted by El Dandachy [43] and subsequently detailed by El Dandachy et al. [40] and Hachem et al. [53], investigated the impact of shear loading on gas conductivity at the rebar-concrete interface. To evaluate these properties, a push-in test setup was utilized (Figure 1). The methodology involved securing the bottom face of a concrete specimen against a rigid support while applying a longitudinal compressive force to the steel rebar, driving it toward the fixed base. This specific configuration was engineered to induce a controlled shear failure at the interface between the steel and the concrete, allowing for precise measurement of gas permeability under mechanical stress.

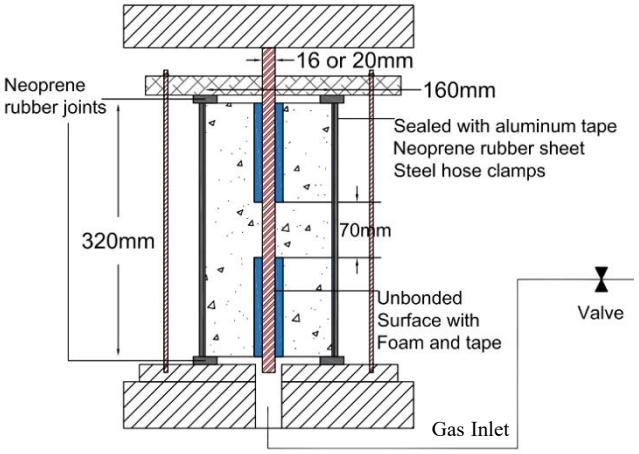

Figure 1. Concept of push-in test [40, 43]

2.2. Material Properties and Specimen Preparation

The reinforced concrete (RC) specimens were cast using a standard mix designed to achieve specific mechanical properties at 28 days. These properties include a compressive strength of 28 MPa, a tensile strength of 2.4 MPa, and a Young's modulus of 29 GPa. The Poisson's ratio for the mix was maintained at 0.2. The detailed concrete mix proportions are summarized in Table 1 below.

Table 1. Concrete Mix Proportions

Components	Quantity (kg/m^3)
Ordinary Portland cement	300
Water	165
Sand 0/4 crushed limestone sand	750
Gravel crushed limestone 6/10	550
Gravel crushed limestone 16/20	550

For the push-in tests, three cylindrical RC samples were prepared, each with dimensions of 160 mm in diameter and 320 mm in height (Figure 2). To ensure the results are representative of industrial applications, specifically pre-stressed concrete containment structures, a 16 mm diameter ribbed steel rebar was selected as the reinforcement. To guarantee a shear failure mode at the steel-concrete interface—rather than a global concrete failure—the effective bond length was limited to L = 70 mm (as illustrated in Figure 3). This reduced interface length aligns with the experimental protocols established in previous literature [35], focusing the mechanical stress specifically on the bond zone.

Figure 2. Three specimens G1, G2, G3

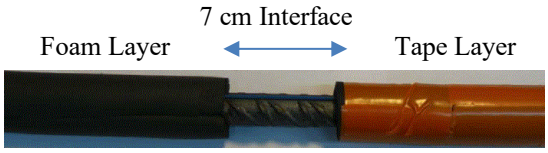

Figure 3. Preparation of the steel rebar using foam sleeves and adhesive tape to define a 7 cm active interface length

2.3. Loading Protocol and Instrumentation

To simulate the mechanical stress at the interface, compressive loading was applied to the steel rebar using a 1 MN hydraulic jack (SCHENK). This high-capacity system enabled the application of both static and cyclic loading regimes with precision.

The test was conducted under displacement control at a constant loading rate of 0.002 mm/s. This slow rate was selected to ensure the stable progression of shear cracks and to allow for continuous monitoring of gas permeability during the loading process. Each push-in test was maintained until complete debonding occurred at the steel-concrete interface, defined as the point where the residual bond strength reached zero.

2.4. Mechanical Behavior

The mechanical response of the specimens during the push-in tests provides critical insight into the progressive bond degradation process. Figure 4 displays an X-ray tomography scan of a specimen captured immediately following the peak shear force, revealing a dense concentration of micro-cracks localized around the reinforcement. This internal imaging confirms that the primary failure mechanism is governed by the shearing of the steel-concrete interface rather than a global structural failure. As illustrated by the load-displacement curves in Figure 5, the interface demonstrates a distinct mechanical progression across samples G1, G2, and G3. An initial elastic phase is characterized by a linear increase in force with minimal displacement, followed by a non-linear transition as the load approaches peak levels—typically between 55 kN and 62 kN. This reduction in stiffness indicates the initiation of micro-cracking near the steel ribs. Following the peak force, a gradual post-peak softening branch is observed, where the load-carrying capacity diminishes as the slip increases. This behavior, characterized by the combination of localized cracking and a controlled reduction in residual strength, reinforces the conclusion that bond failure in this push-in configuration is a progressive process driven by gradual damage near the steel-concrete boundary.

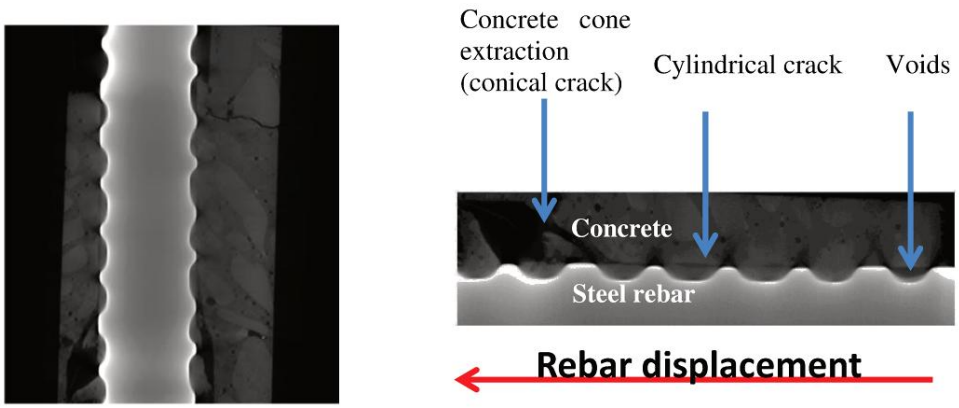

Figure 4. Section of the reinforced specimen subjected to shear loading at the interface provided by x-ray tomography just after the peak force

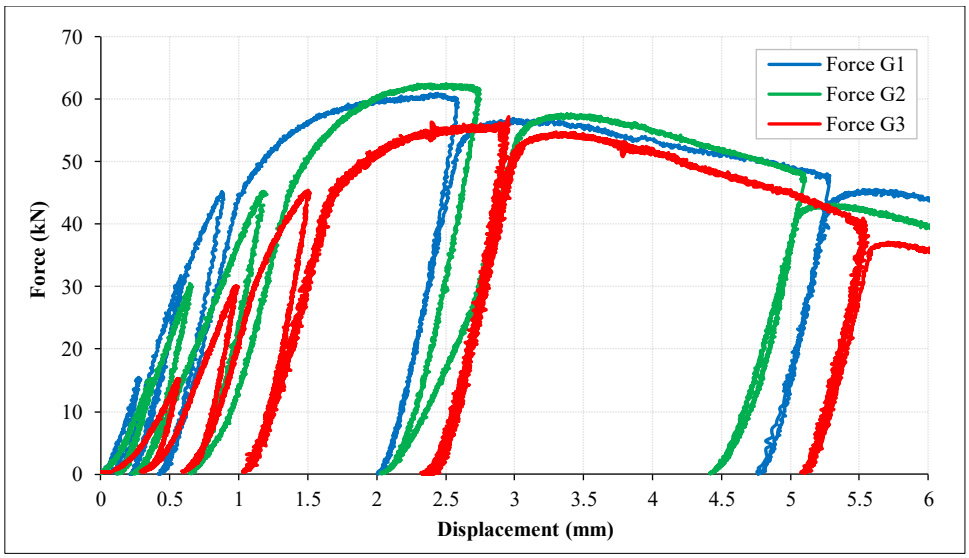

Figure 5. Mechanical response of the steel rebar-concrete interface during push-in test

Although the experimental program is limited to three specimens, this sample size is consistent with similar bond behavior studies where experiments are primarily used for numerical model calibration rather than statistical generalization. The subsequent parametric analysis extends the applicability of the findings across a broader range of conditions.

3. Finite Element Analysis (FEA)

To further validate the experimental findings and provide a comprehensive understanding of the push-in test behavior, numerical simulations were performed using Finite Element Analysis (FEA). The research methodology is structured as an integrated workflow, transitioning from the experimental baseline to a comprehensive numerical investigation, as illustrated in the flowchart in Figure 6.

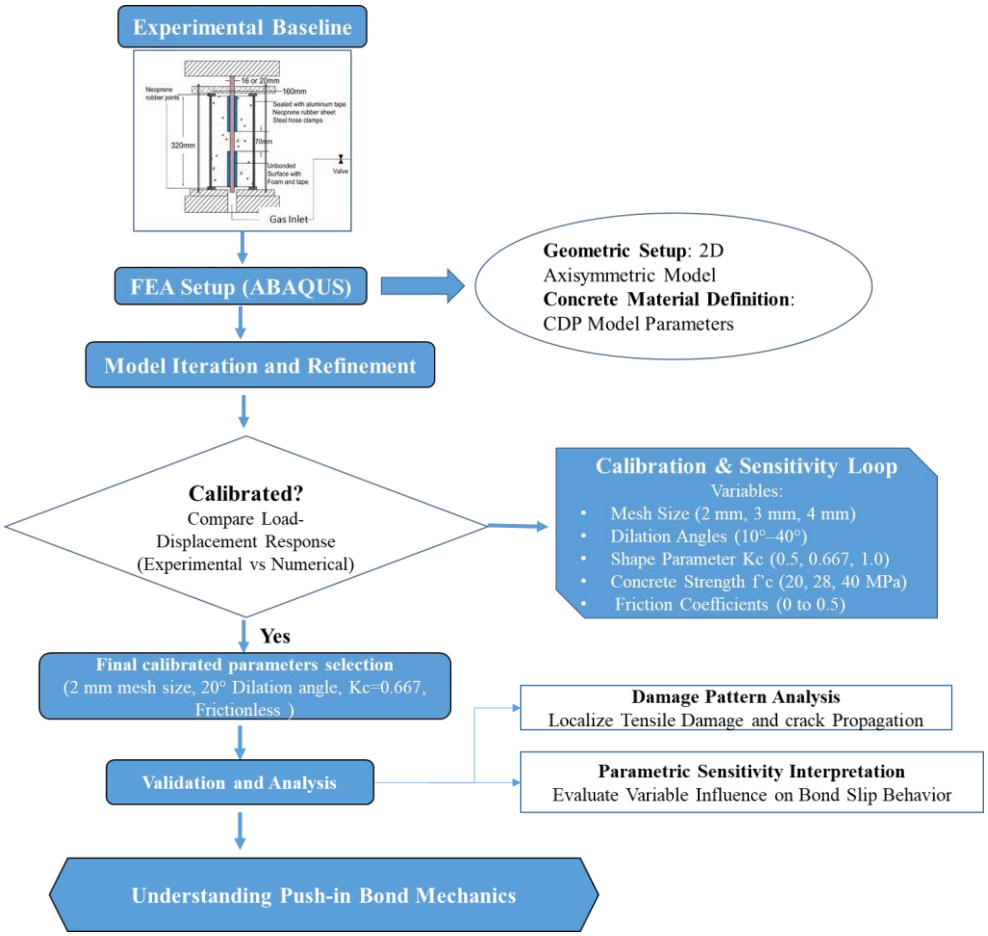

Figure 6. Integrated experimental-numerical methodology flowchart for the analysis of push-in bond mechanics

These simulations were designed to replicate the laboratory conditions and explore additional variables that are difficult to isolate physically. Calibrated models in ABAQUS were employed to simulate stress distribution and bond failure mechanisms, building upon established literature [54, 55]. The development of these models followed an iterative calibration and sensitivity analysis loop, systematically evaluating parameters such as mesh discretization, concrete dilation angles, the yield surface shape parameter (Kc), interface friction, and concrete compressive strength ($f'c$).

3.1. Numerical Methodology and Model Development

The extensive experimental dataset provided a robust baseline for comparison with numerical results. An axisymmetric model was developed within the ABAQUS environment to represent the steel-concrete interface, taking advantage of the geometric, loading, and boundary condition symmetries. While the global response accounts for nonlinearities, the initial material behavior was characterized through the properties summarized in Table 2 [56-58].

Table 2. Materials Properties for FEA

Material Properties	Values
Concrete Poisson's ratio	0.2
Steel Young's modulus	210 GPa
Steel Poisson's ratio	0.3
Steel yield strength	500 MPa

A parametric investigation was conducted to identify potential failure modes. Key variables, including concrete compressive strength ($f'c$), embedded length, dilation angle, and the coefficient of friction, were systematically varied to assess their influence on the bond strengthening efficiency.

3.2. Material Constitutive Models (CDP)

The Concrete Damage Plasticity (CDP) model was utilized to represent concrete behavior, incorporating a fracture energy (g_f) of 5 N/mm. The plasticity parameters were defined with a stress ratio ($\sigma_{b0} / \sigma_{c0}$) of 1.16 and an eccentricity (e) of 0.1, consistent with verified literature [55, 56]. Under tension, the uniaxial stress-strain response was assumed to be linear elastic up to the point of tensile strength, followed by a softening branch as detailed in Appendix I (Figure A1). Under compression, the constitutive response followed the Hognestad-type stress–strain relationship shown in Figure A2, while the evolution of tensile and compressive damage variables was defined according to Figures I.3 and I.4, respectively.

The fracture energy (G_f = 5 N/mm) was selected based on recommendations from the *fib* Model Code 2010, which relates G_f to the maximum aggregate size and the mean concrete compressive strength ($f'c$). This selection ensures a physically consistent representation of concrete cracking behavior. As illustrated by the tensile stress-crack width relationship in Figure A1, G_f dictates the energy dissipation capacity during the post-peak phase; higher values reflect greater ductility, whereas lower values represent a more brittle, sudden degradation of the concrete matrix. Sensitivity analyses performed during model development indicated that while the peak load capacity shows moderate sensitivity to G_f, the transition from stable interfacial slip to splitting failure is dominated by the concrete's dilation angle. The chosen value of 5 N/mm provided the most accurate correlation with the experimental softening branches observed in this study.

3.3. Finite Element Selection and Mesh Sensitivity

To accurately capture the complex stress distribution and geometric nuances within the bond zone, the Finite Element size was selected to be sufficiently small to ensure numerical convergence. A comprehensive mesh sensitivity study was conducted by evaluating three distinct element sizes: 2 mm, 3 mm, and 4 mm. As illustrated in Figure 7, these variations allowed for a detailed assessment of the model's spatial discretization. The 2 mm mesh, in particular, provided a refined representation of the concrete section immediately adjacent to the rebar, which is essential for capturing the high-gradient stress concentrations and localized cracking identified in the experimental tomography scans. This approach ensures that the numerical results remain independent of the mesh density while maintaining computational efficiency [57].

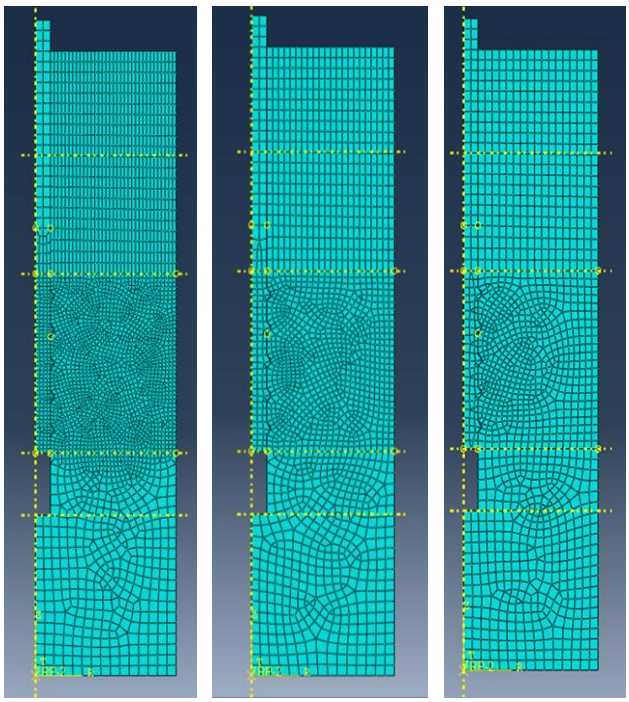

(a) (b) (c)

Figure 7. Steel-concrete meshing (a) 2 mm, (b) 3 mm, (c) 4 mm

3.4. Boundary Conditions and Interactions

To accurately simulate the load, transfer across the reinforcement-concrete boundary, defining precise boundary conditions and contact interactions is essential. As shown in Figure 8, the numerical model incorporates an axisymmetric configuration where the base plate is fully restricted against longitudinal movement and all rotational degrees of freedom. The mechanical loading is introduced via a vertical displacement applied to the top of the steel rebar, simulating the axial push-in force used in the experimental setup. The interactions between the base plate and the concrete base, as well as the critical interface between the steel rebar and the surrounding concrete, were defined using a surface-to-surface contact formulation. For tangential behavior, Coulomb's friction law was implemented to account for the physical roughness of the materials. To calibrate the model against laboratory findings, the friction coefficient was systematically varied between 0 and 0.5 to identify the value providing the highest correlation with experimental measurements. The normal behavior of the contact surfaces was defined using a "hard" contact model. This formulation prevents any numerical penetration of the surfaces while allowing for potential separation after contact, ensuring a realistic representation of the interface mechanics during the debonding process. Notably, the choice of a frictionless tangential behavior ($\mu = 0$) in the final calibrated model ensures that the resistance is governed solely by the mechanical interlocking of the rebar ribs, which are explicitly represented in the 2D axisymmetric geometry. This approach avoids the overestimation of bond capacity that often occurs through redundant frictional forces when rib geometry is already present in the mesh.

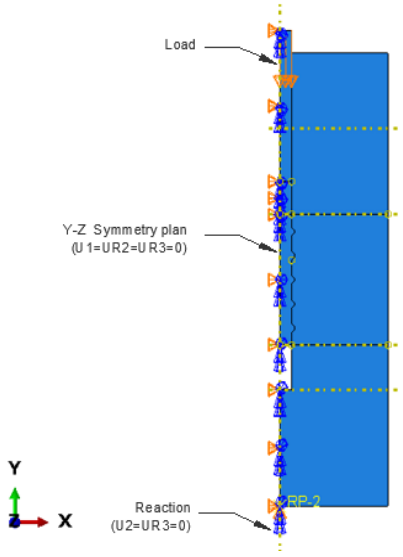

Figure 8. Boundary conditions

3.5. Parametric Study and Model Calibration

To rigorously evaluate the sensitivity of the Concrete Damage Plasticity (CDP) model and ensure its alignment with physical observations, a comprehensive suite of 36 simulations was executed. This matrix investigated the influence of several critical parameters, including mesh discretization, dilation angles, the yield surface shape parameter (Kc), the interface friction coefficient, and the concrete grade. The specific combination of parameters that yielded a good correlation with the experimental load-displacement response, is summarized in Table 3.

Table 3. Concrete Material and Interface Parameters

Parameter	Unit	Calibrated Value
Compressive Strength (f'c)	MPa	28
Young's Modulus (E)	GPa	29
Dilation Angle (ψ)	°	20
Yield Surface Shape (Kc)	-	0.6667
Fracture Energy (Gf)	N/mm	5
Interface Friction	-	Frictionless

Two distinct numerical approaches were compared using the three experimental cylinders as control specimens: a static analysis via ABAQUS/Standard and a quasi-static analysis via ABAQUS/Explicit.

The comparative load-displacement responses for the experimental, static, and quasi-static studies are illustrated in Figure 9. While both numerical methods successfully capture the general mechanical behavior and softening branch, slight variations are observed in terms of the ultimate load and corresponding deflection. Specifically, the numerical models exhibit a higher initial stiffness compared to the average experimental test results, though they accurately converge toward the residual strength levels observed during the post-peak phase. This comprehensive parametric study provides a deeper understanding of the stress redistribution mechanisms occurring at the rebar-concrete interface throughout the loading history.

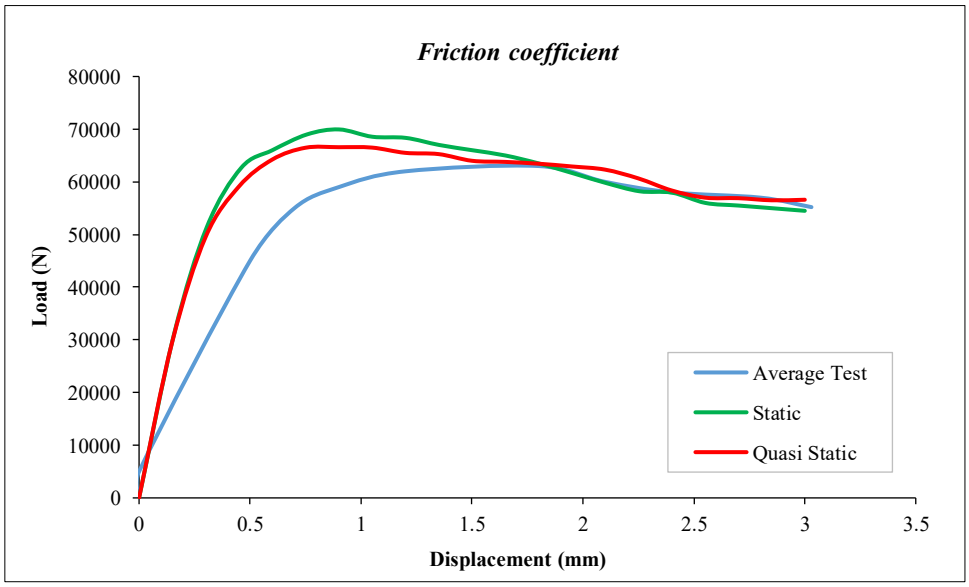

Figure 9. Load-displacement response by comparing static and quasi-static analysis

3.5.1. Mesh Sensitivity Analysis

To ensure the reliability of the numerical results and investigate the influence of spatial discretization on the model's performance, a mesh convergence study was performed. In Finite Element modelling of concrete, the mesh size directly impacts the width of the localization band; while a finer mesh typically provides higher resolution, excessive refinement can lead to numerical instabilities or non-convergence as the equations approach a singularity.

As illustrated in Figure 10, three distinct element sizes—2 mm, 3 mm, and 4 mm—were evaluated. The results indicate that while the ultimate failure load remains relatively consistent across all tested mesh densities, the failure displacements and post-peak softening behavior are highly sensitive to the element size. The 2 mm mesh provided the most accurate correlation with the experimental data, effectively capturing the localized cracking behavior observed in the physical specimens. Consequently, a 2 mm mesh size was adopted for all subsequent simulations to ensure an optimal balance between computational efficiency and predictive accuracy. To provide a quantitative justification for the mesh selection, the performance of the three mesh densities was evaluated in terms of peak load (Fu) and the corresponding displacement at peak load (δu). As shown in Table 4, the 2 mm mesh provides the closest correlation with the experimental 'Average test' curve. The 3 mm and 4 mm mesh sizes overestimate the peak load by approximately 6.1% and 10.6%, respectively. This deviation confirms that the 2 mm discretization is necessary to prevent numerical overestimation of bond capacity and to accurately capture the experimental softening response.

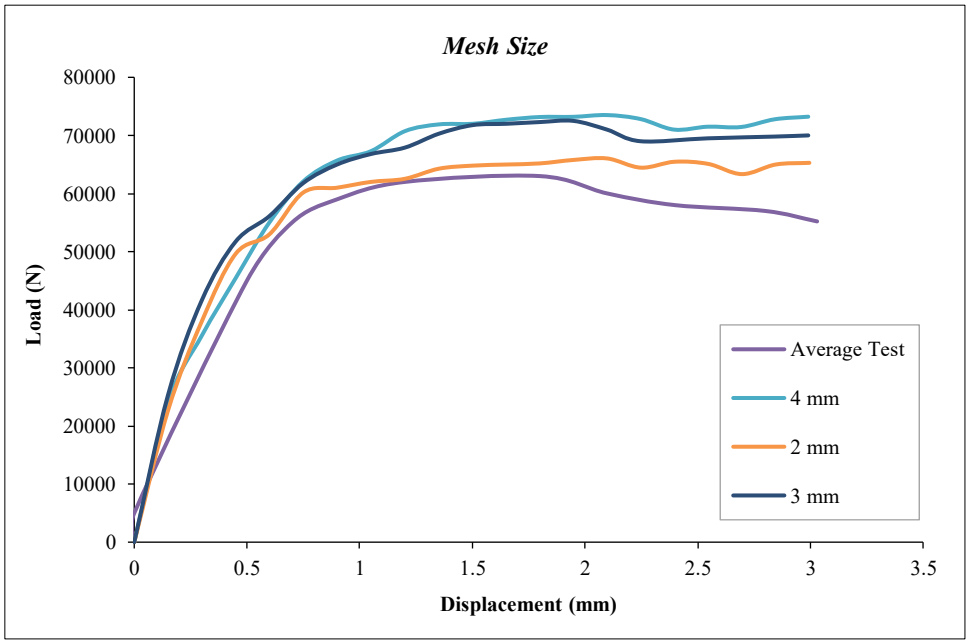

Figure 10. Load displacement response by comparing mesh sizes

Table 4. Quantitative comparison of numerical results across varying mesh sizes

Mesh Size (mm)	Peak Load (Fu, N)	Difference from 2mm (%)	Displacement at Peak (δu, mm)	Difference from 2mm (%)
2	66,000	—	2.1	—
3	70,000	6.06%	2	4.76%
4	73,000	10.61%	1.9	9.52%

3.5.2. Influence of Dilation Angle

Due to its inherently brittle nature, concrete undergoes dilatancy—significant volume changes induced by inelastic stresses—during mechanical loading. Within the Concrete Damage Plasticity (CDP) framework, this phenomenon is governed by the dilation angle, which fundamentally influences the confinement and resultant frictional forces at the steel-concrete interface. Theoretically, a higher dilation angle enhances the interlocking effect, thereby increasing the peak stress required to drive the rebar into the concrete specimen. To determine the optimal value for this critical parameter, a sensitivity analysis was conducted using a range of dilation angles from 10° to 40°. The comparative load-displacement responses are illustrated in Figure 11. The results demonstrate that as the dilation angle increases, the model predicts higher peak loads due to the increased confinement pressure at the interface. Among the values tested, a dilation angle of 20° provided the closest correlation to the experimental peak stress and softening behavior. While higher angles (30° and 40°) significantly overestimated the ultimate bond capacity, the 20° model accurately captured the transition from elastic loading to interface failure. Consequently, 20° was selected as the calibrated dilation angle for all further numerical investigations.

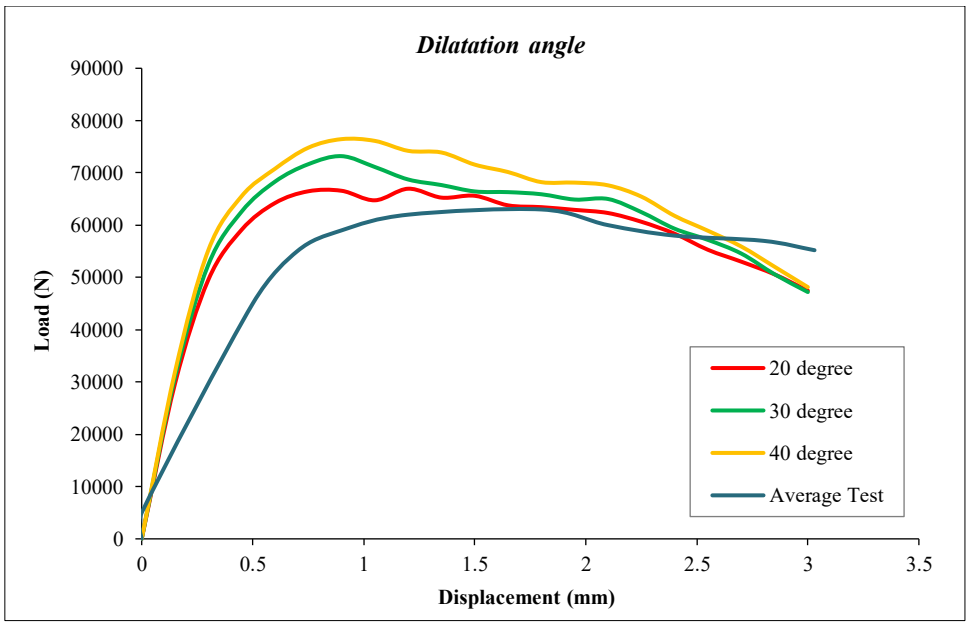

Figure 11. Load-displacement response by comparing Dilation angles

3.5.3. Influence of Yield Surface Shape Parameter (K_C)

The yield surface shape parameter, K_c, is a critical coefficient in the Concrete Damage Plasticity (CDP) model that defines the ratio of the distances from the hydrostatic axis to the yield surface in triaxial compression and tension. To maintain a convex yield surface, the parameter must strictly satisfy the condition $0.5 < Kc \leq 1$, with the ABAQUS default typically set at 0.6667. To evaluate the influence of this geometric factor on the bond behavior, sensitivity analyses were performed using three discrete values: 0.5, 0.6667, and 1.0. The resulting load-displacement curves are presented in Figure 12.

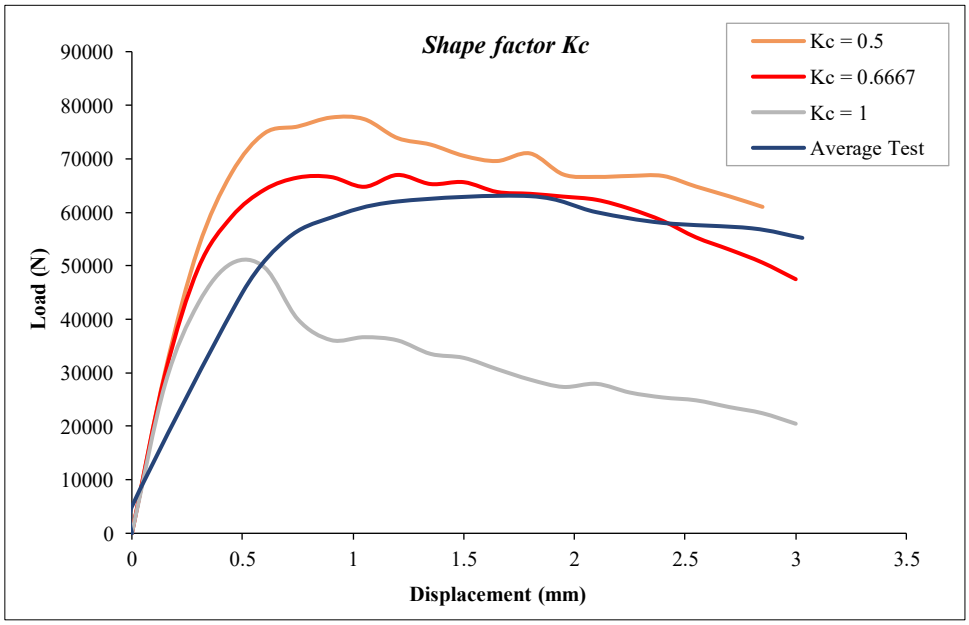

Figure 12. Load-displacement response comparing shape factor (Kc)

The data indicate that lower values of K_c (e.g., 0.5) induce a sharper transition from elastic to plastic behavior, leading to a sudden softening branch immediately following the peak stress. Conversely, a value of Kc = 1.0, which represents a Rankine-type circular yield surface in the deviatoric plane, significantly underestimates the ultimate capacity and fails to capture the ductility of the interface. As shown in the comparison, a shape factor of 0.6667 facilitates a smoother stress-strain transition and a more realistic post-peak softening response, aligning closely with the experimental "Average Test" curve. While it results in a slightly stiffer initial response than the physical specimens, it provides the best numerical stability and predictive accuracy for the ultimate load. Consequently, Kc = 0.6667 was adopted for all subsequent modelling phases.

3.5.4. Influence of Tangential Friction

The tangential friction coefficient at the rebar-concrete interface significantly influences the simulated bond strength, specifically by increasing the peak load and delaying the post-peak softening behavior. To determine the most representative interaction model, a sensitivity analysis was performed with friction coefficients ranging from 0 (frictionless) to 1.4. The comparative load-displacement responses are presented in Figure 12. The numerical results indicate that any friction coefficient exceeding 0.5 leads to a substantial overestimation of the bond stress, with values reaching up to 1.4 times the experimental measurements. This elevated stress level across the entire curve is attributed to the enhanced force transfer mechanism provided by the frictional resistance in the model.

As illustrated in Figure 13, the frictionless model ($\mu = 0$) provides the highest degree of correlation with the experimental "Average Test" behavior. This suggests that for this specific push-in configuration, the mechanical interlocking of the ribs—already accounted for by the geometry and the Concrete Damage Plasticity parameters—is the primary driver of resistance, while pure surface friction plays a negligible role in the initial capacity. Consequently, a frictionless interface was adopted for all subsequent numerical investigations.

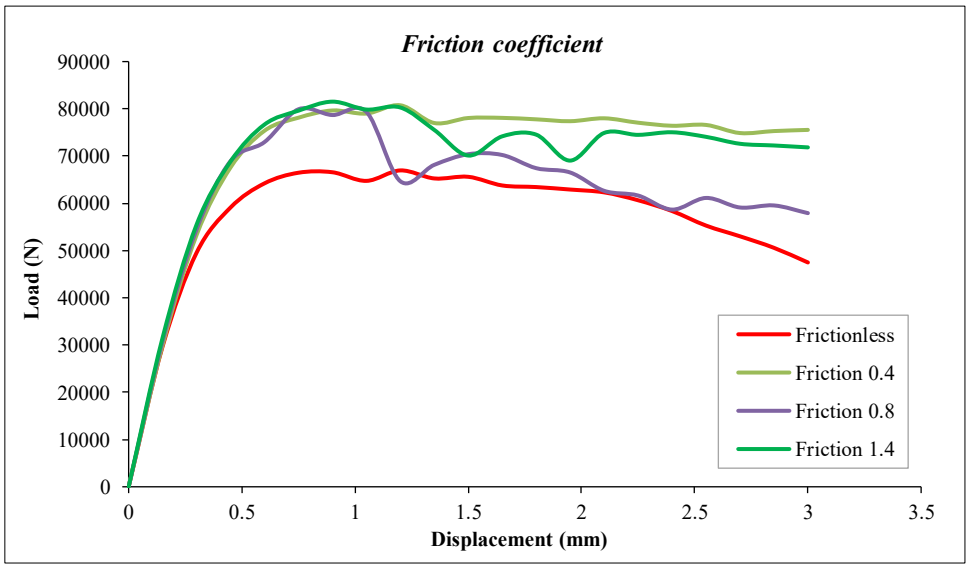

Figure 13. Load-displacement response comparing friction coefficient

3.5.5. Influence of Concrete Compressive Strength (*f'c*)

To investigate the sensitivity of the bond-slip mechanism to the quality of the concrete matrix, three distinct compressive strength values—20 MPa, 28 MPa, and 40 MPa—were evaluated. As illustrated in Figure 14, the ultimate load capacity of the steel-concrete interface increases proportionally with the compressive strength of the concrete. Specifically, the cylinders with *f'c* values of 28 MPa and 40 MPa exhibited significantly higher ultimate loads compared to the 20 MPa baseline. This trend aligns with the theoretical understanding that a higher-strength matrix provides greater resistance to the localized crushing and micro-cracking occurring at the rebar ribs.

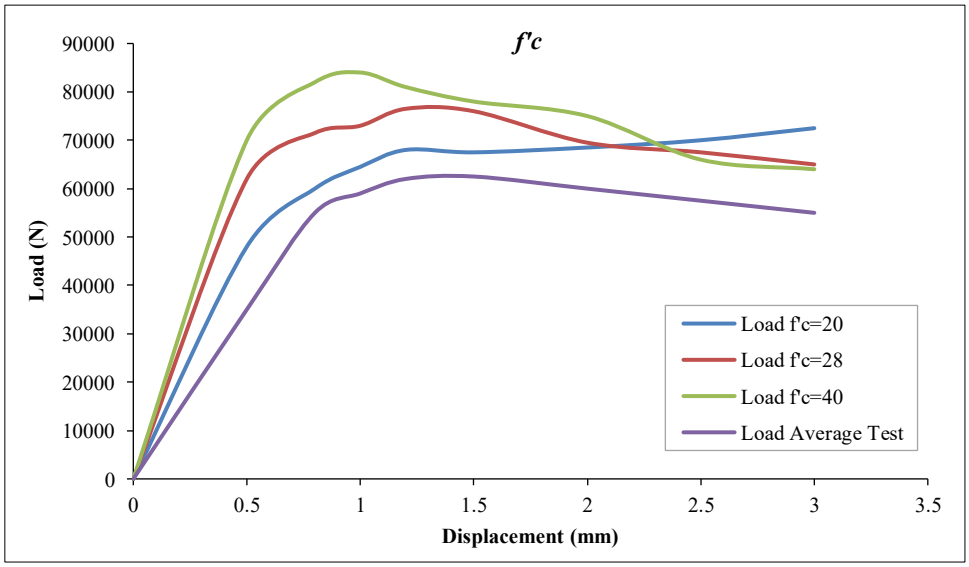

Figure 14. Effect of *f'c* on load-displacement curves

However, it is important to note that the Finite Element (FE) analysis consistently predicts a stiffer response and a slightly higher ultimate capacity than the average experimental results. This observed overestimation in the numerical model can be attributed to the elevated level of confinement achieved by the radial strain exerted by the steel rebar in the idealized axisymmetric environment, which may be more pronounced than in the physical laboratory specimens.

The systematic parametric investigation has identified the optimal numerical configuration for simulating the push-in test. By selecting a 2 mm mesh size, a dilation angle of 20°, a shape factor (K_c) of 0.6667, and a frictionless interface, the model achieves a robust balance between numerical stability and experimental correlation.

4. Results and Discussion

4.1. Numerical Validation and Parameter Sensitivity Analysis

The numerical load-displacement response obtained using the Concrete Damage Plasticity (CDP) model demonstrates a high degree of correlation with the experimental average results in Figure 15, with discrepancies in ultimate load and failure displacement consistently below 10%. However, the model exhibits a persistent tendency to overestimate strength throughout the loading history, a phenomenon frequently reported in studies utilizing the CDP framework for bond-slip analysis [59-62]. Furthermore, recent numerical investigations by Nasiri et al. [63] corroborate that while the CDP approach is effective for simulating complex structural behaviors, it requires meticulous calibration of material parameters to accurately replicate post-peak softening. This numerical overestimation is primarily attributed to three fundamental modeling assumptions: the assumption of a perfectly homogeneous concrete matrix compared to the micro-voids present in physical specimens, the restrictive uniform radial confinement of the 2D axisymmetric representation, and the inherent limitations of the standard CDP framework regarding post-peak softening compared to more advanced constitutive models like CDPM2 [62]. When compared to standard pull-out test literature [17, 23], our push-in results demonstrate a higher initial stiffness, which is physically consistent with the "compressive confinement effect" unique to push-in configurations. Whereas pull-out tests subject the concrete to tensile hoop stresses that facilitate earlier cracking, the push-in setup leverages the lateral expansion of the concrete against the rigid base, effectively delaying the onset of interfacial damage. Consequently, the model's ability to capture this transition, despite its idealized geometry, validates the adopted strategy and confirms that the push-in configuration provides a distinct, more confined stress state than traditional bond characterization methods.

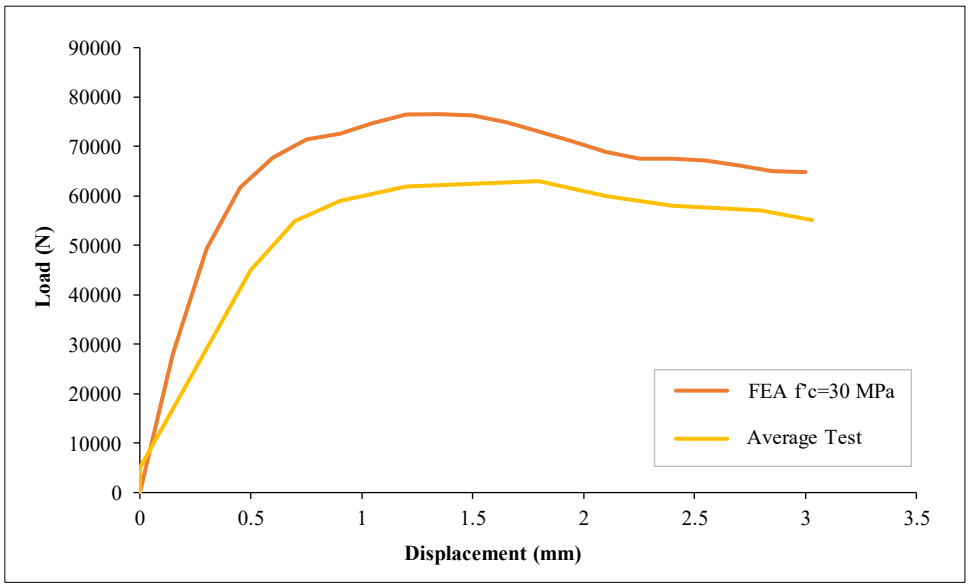

Figure 15. Load-displacement curve

The progression of concrete damage, specifically the initiation and propagation of tensile cracking, is detailed across various mesh densities in Figures 16 to 18. A comparative analysis of these damage patterns confirms that the specimen loses strength progressively as the reinforcement slips, with the 2 mm mesh configuration (Figure 15) clearly localizing tensile damage at the interface between the rebar ribs and the surrounding concrete. As the load approaches its ultimate capacity, these cracks propagate radially, signifying the crushing of the concrete keys between the ribs—a localized failure mode consistent with the push-in behavior observed in experimental tests. The high degree of morphological similarity between these predicted crack patterns and experimental findings confirms that the model accurately captures the internal stress redistribution during the bond-slip process. Beyond validation, these findings hold significant implications for structural design: the concentration of tensile damage at the interface zone underscores the necessity of concrete confinement in critical elements, such as beam-column joints in seismic regions. The radial cracking observed in Figure 15c serves as a mechanical precursor to brittle splitting failure, which can be mitigated through adequate concrete cover or transverse reinforcement. By linking the finite element contours to specific failure modes, this study

provides a clear visualization of how bond integrity influences structural safety. To quantify these influences, a comprehensive parametric investigation was conducted, isolating key variables—dilation angles (10°–40°), anchorage lengths (5–9 cm), and concrete compressive strengths (20–40 MPa)—to determine their impact on bond strength. These parameters were selected to represent a broad spectrum of structural design requirements, and a dynamic solution protocol was utilized to ensure numerical stability during the nonlinear degradation of the bond.

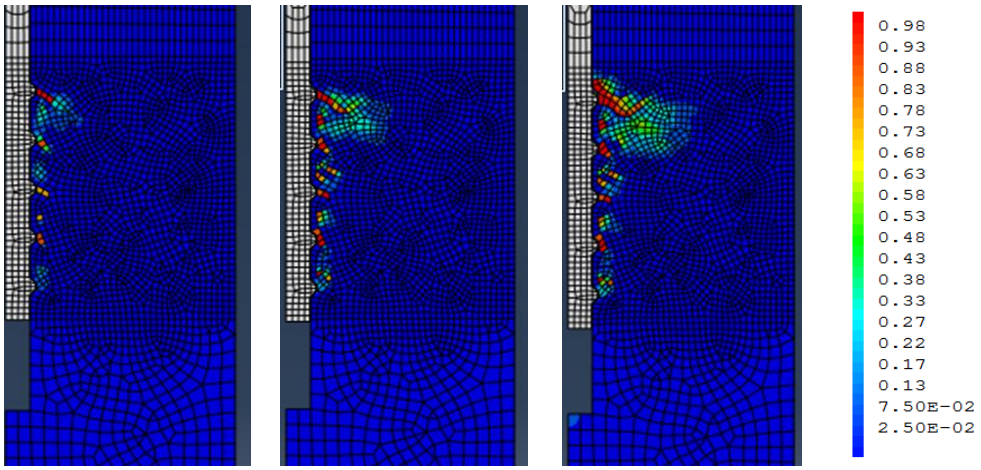

(a) (b) (c)

Figure 16. Tensile damage pattern for mesh size = 2 mm (a) before the ultimate load (b) at the ultimate load (c) after the ultimate load

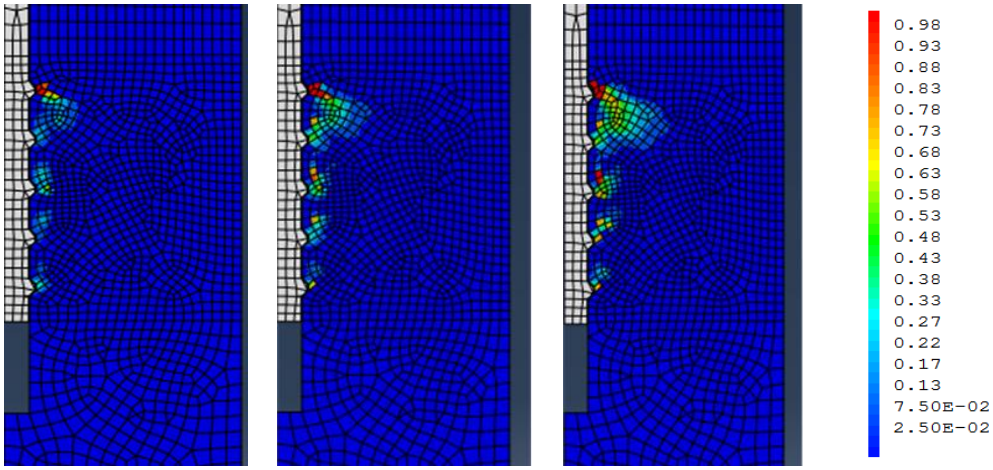

(a) (b) (c)

Figure 17. Tensile damage pattern for mesh size = 3 mm (a) before the ultimate load (b) at the ultimate load (c) after the ultimate load

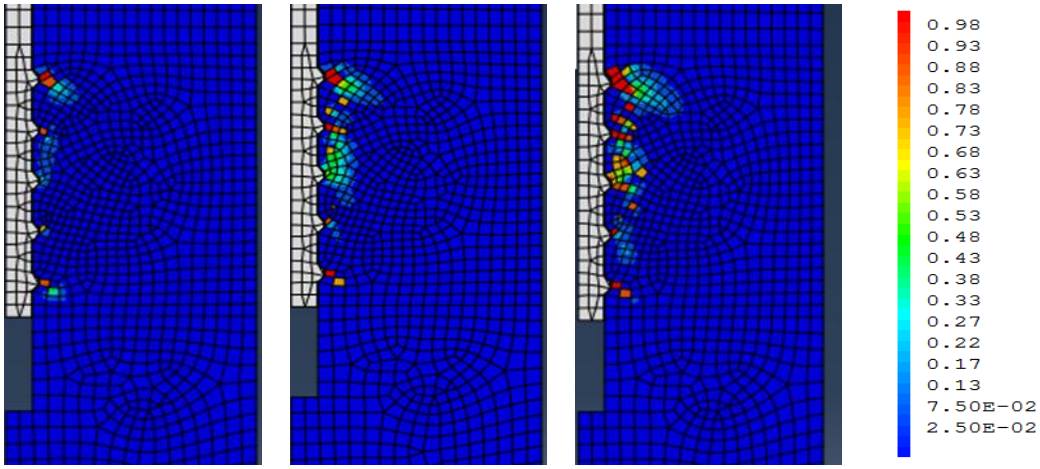

(a) (b) (c)

Figure 18. Tensile damage pattern for mesh size = 4mm (a) before the ultimate load (b) at the ultimate load (c) after the ultimate load

4.2. Influence of Concrete Compressive Strength and Dilatation on Ultimate Capacity

The relationship between concrete compressive strength (*f'c*) and the ultimate load-bearing capacity is illustrated in Figure 19 for a constant anchorage length of 7 cm. The data exhibits a consistent positive correlation, where increments in *f'c* consistently enhance the ultimate load across all tested dilation angles. Notably, at *f'c* = 28 MPa, the ultimate load increases by approximately 31% as the dilation angle is scaled from 10° to 40°. This trend is replicated across the 20 MPa and 40 MPa series, suggesting that the bond's sensitivity to concrete quality is significantly amplified by the material's volumetric expansion characteristics.

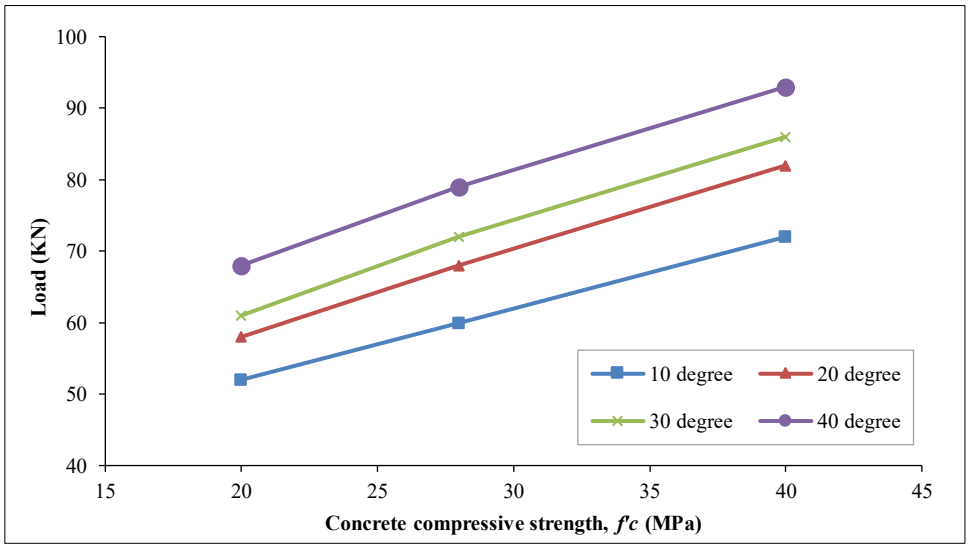

Figure 19. Effect of concrete compressive strength on ultimate load for different dilation angles for L=7 cm

The observed increase in load-bearing capacity at higher dilation angles is attributed to the mechanics of lateral expansion under axial loading. Within the confined push-in configuration, a higher dilation angle increases the concrete's propensity for lateral expansion against the rigid surrounding matrix. This generates intensified radial confinement pressures against the reinforcement ribs, thereby enhancing the frictional component of the bond and effectively delaying the onset of interfacial slip. This mechanism promotes a more uniform stress distribution across the interface, enabling the assembly to sustain higher axial loads prior to reaching the failure threshold. This behavior is further substantiated by the multi-variable analysis in Figure 20, which compares the interplay of *f'c* and dilation across anchorage lengths of 5, 7, and 9 cm. While absolute capacity is primarily governed by anchorage length and concrete grade, the dilation angle acts as a critical secondary factor regulating both the initial stiffness and peak bond capacity.

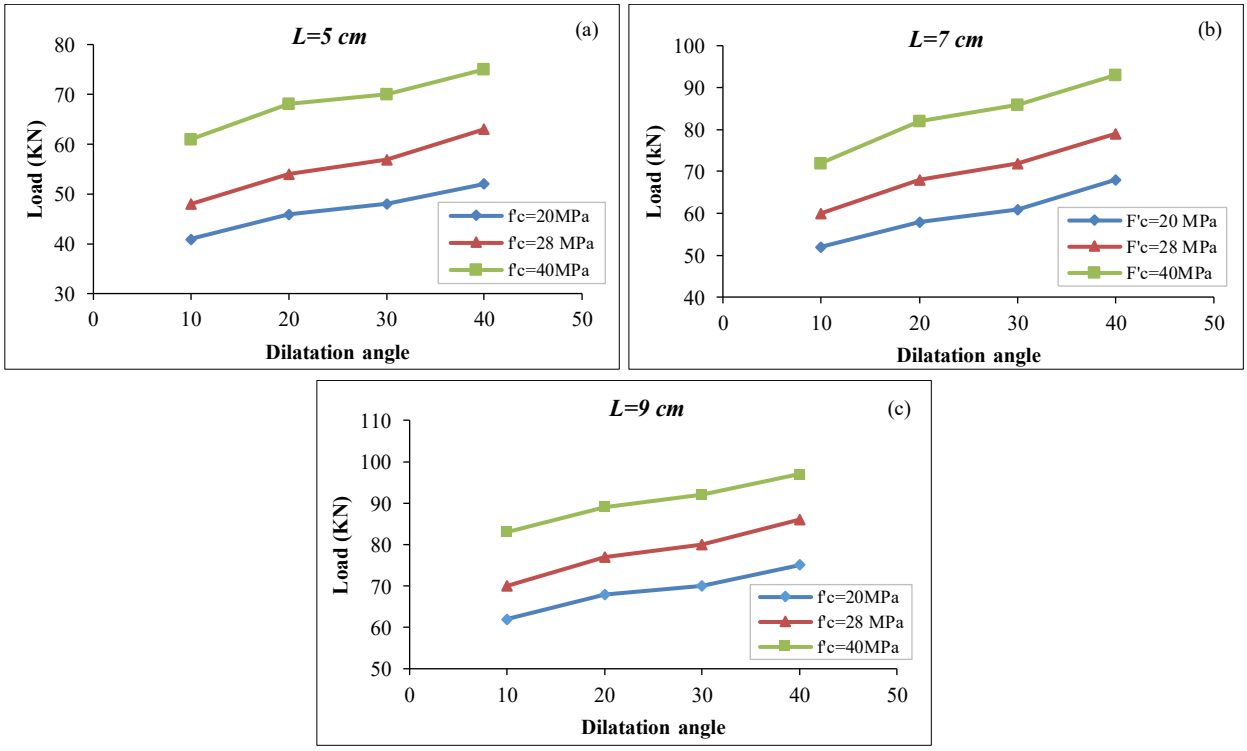

Figure 20. Effect of *f'c* and dilation on the ultimate load a) L= 5cm, b) L= 7cm, c) L= 9cm

However, this relationship is inherently non-linear; while moderate dilation values (typically 20°–30°) yield results consistent with documented interface behavior [35, 55], extreme values tend to overestimate bond capacity due to idealized confinement effects. Consequently, these findings highlight that in push-in configurations—which inherently emphasize compressive confinement compared to traditional pull-out tests—the dilation angle is a primary sensitivity parameter.

4.3. Influence of Concrete Compressive Strength and Anchorage Length on Bond Performance

The combined effect of concrete compressive strength (*f'c*) and embedded length (L) on the ultimate bond capacity is illustrated in Figure 21, categorized by the four investigated dilation angles (10° to 40°). The results demonstrate a consistent linear growth in ultimate load as the compressive strength increases from 20 to 40 MPa, regardless of the anchorage length or dilation characteristics. This trend confirms that the mechanical properties of the concrete matrix remain the primary driver of peak load-bearing capacity, as higher-strength concrete provides greater resistance against the localized crushing at the rebar rib interface. A quantitative assessment of the embedded length reveals its critical role in enhancing bond strength through increased mechanical interlock and frictional surface area. For a concrete strength of 28 MPa and a dilation angle of 30°, the ultimate load increases by approximately 26% when extending the length from 5 cm to 7 cm, and by 11% when further increasing the length to 9 cm. Overall, a 30% increase in capacity is observed when comparing the 5 cm and 9 cm embedded lengths.

This diminishing rate of return suggests that while increasing the interface length provides more surface area for the steel-concrete interaction, the bond stress distribution becomes increasingly non-uniform over longer lengths, with the highest stress concentrations remaining near the loaded end. This indicates that the contribution of additional embedment length becomes progressively less effective due to the non-uniform stress distribution along the interface. This phenomenon is observed across all tested compressive strengths and dilation angles, validating the assumption that anchorage length is a fundamental geometric constraint on structural safety. By increasing the embedded length, the structural assembly can mobilize a larger volume of concrete to resist the push-in force, thereby elevating the load threshold before a catastrophic slip occurs. These findings highlight that optimized design for structural joints should balance concrete grade and anchorage length to ensure robust bond performance, particularly in seismic applications where load redistribution is critical. This behavior confirms that increasing embedment length does not necessarily lead to proportional gains in bond strength, highlighting the importance of optimized design rather than simply increasing anchorage length.

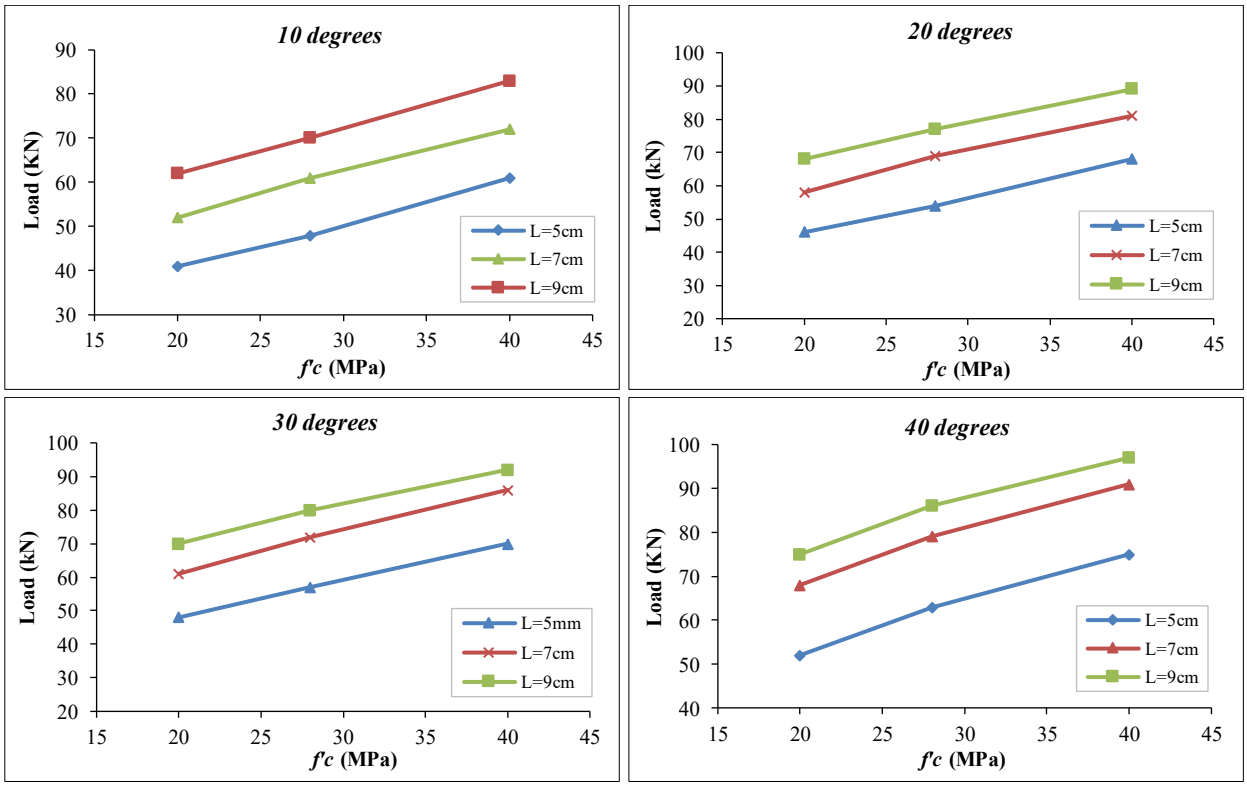

Figure 21. Effect of concrete compressive strength on the ultimate load in relation to the embedded lengths a) 10 degrees, b) 20 degrees, c) 30 degrees, d) 40 degrees

Furthermore, the non-uniform bond stress distribution observed along the anchorage length is significantly influenced by the boundary conditions inherent to the push-in configuration. The interaction between end friction and lateral inertial confinement serves as a primary mechanical constraint, dictating the stress transmission and the ultimate bond capacity. These boundary effects are critical, as documented in recent research [66], confirming that the observed load-bearing performance is not merely a function of material properties but is intrinsically linked to the confinement mechanisms established at the interface and the base of the specimen.

4.4. Influence of Embedment Length and Compressive Strength on Average Bond Stress

A key outcome of this study is the identification of a critical embedment length governing bond efficiency. The interplay between embedment length (L) and concrete compressive strength ($f'c$) is further evaluated in Figure 22 to determine the efficiency of the bond interface. For this analysis, three distinct compressive strength values (20, 28, and 40 MPa) were simulated using a constant dilation angle of 20°. The results indicate that while the absolute ultimate load generally follows an upward trend with the increase of $f'c$—showing an approximate 19% increase when moving from 20 MPa to 28 MPa at L = 7 cm—the average bond stress (N/mm^2) exhibits a non-linear relationship. Specifically, the data demonstrates that increasing the embedded length from 5 cm to 7 cm enhances the bond efficiency, yet a subsequent increase to 9 cm results in a noticeable reduction in the average bond stress. This observed decrease in average stress beyond an embedment length of 7 cm suggests a critical threshold in the bond-slip mechanism. While a longer interface typically provides more surface area for mechanical interlock, it also alters the internal stress distribution, potentially leading to a shift in the failure mode. In the 9 cm specimens, a transition from gradual interface cracking to a more brittle splitting failure may be initiated, as the increased length allows for the accumulation of higher radial stresses that exceed the tensile capacity of the concrete cover. This phenomenon implies that there is an optimal anchorage length for specific concrete grades, beyond which the gain in surface area is offset by the non-uniform distribution of bond stresses and the risk of premature splitting. These observations are fundamental for structural engineers in determining the most efficient anchorage details for ensuring ductility and safety in reinforced concrete connections.

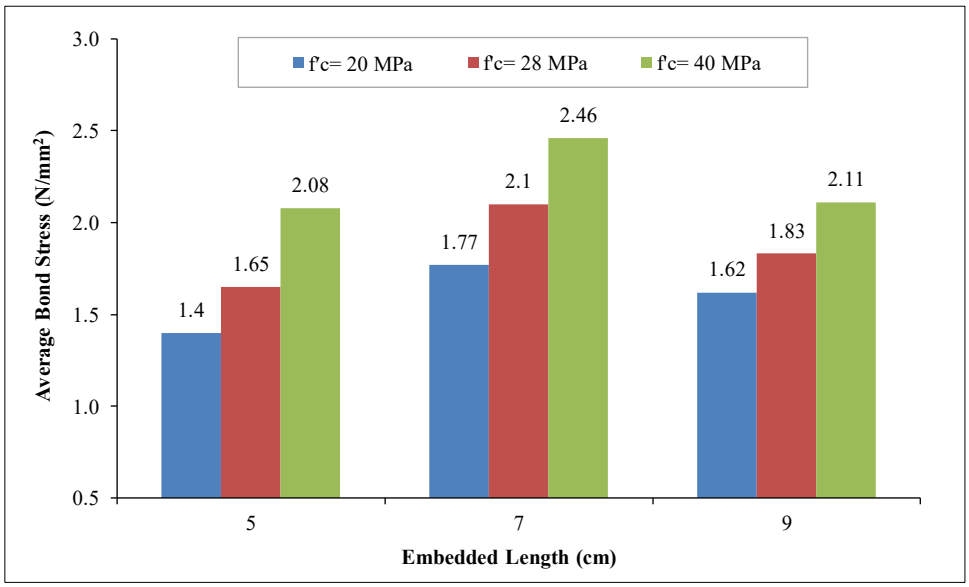

Figure 22. Influence of embedded length (L) on the average bond stress for varying concrete compressive strengths ($f'c$) at a constant 20° dilation angle

Furthermore, the non-uniform bond stress distribution and the identified threshold at 7 cm are significantly influenced by the boundary conditions inherent to the push-in configuration. The interaction between end friction and lateral inertial confinement serves as a primary mechanical constraint, dictating the stress transmission and the ultimate bond capacity. These boundary effects are critical, as documented in recent research [64], confirming that the observed load-bearing performance is not merely a function of material properties but is intrinsically linked to the confinement mechanisms established at the interface and the base of the specimen. Consequently, the transition to brittle splitting at higher embedment lengths is a direct consequence of these localized stress concentrations, reinforcing the findings of previous comparative studies on interfacial bond characterization [17, 23].

4.5. Non-linear Influence of Dilation and Confinement on Bond Capacity

The relationship between the dilation angle, embedded length, and ultimate load capacity is further examined in Figure 23. The data reveals a distinct non-linear sensitivity to the dilation angle across all concrete compressive

strengths. Specifically, a substantial increase in ultimate load is observed when transitioning from 10° to 20°, followed by a localized plateau or moderate gain between 20° and 30°, and finally a sharp secondary increase from 30° to 40°. This step-like progression in capacity suggests a complex mechanical interplay between the material's volumetric expansion and the resulting passive confinement provided by the surrounding concrete matrix.

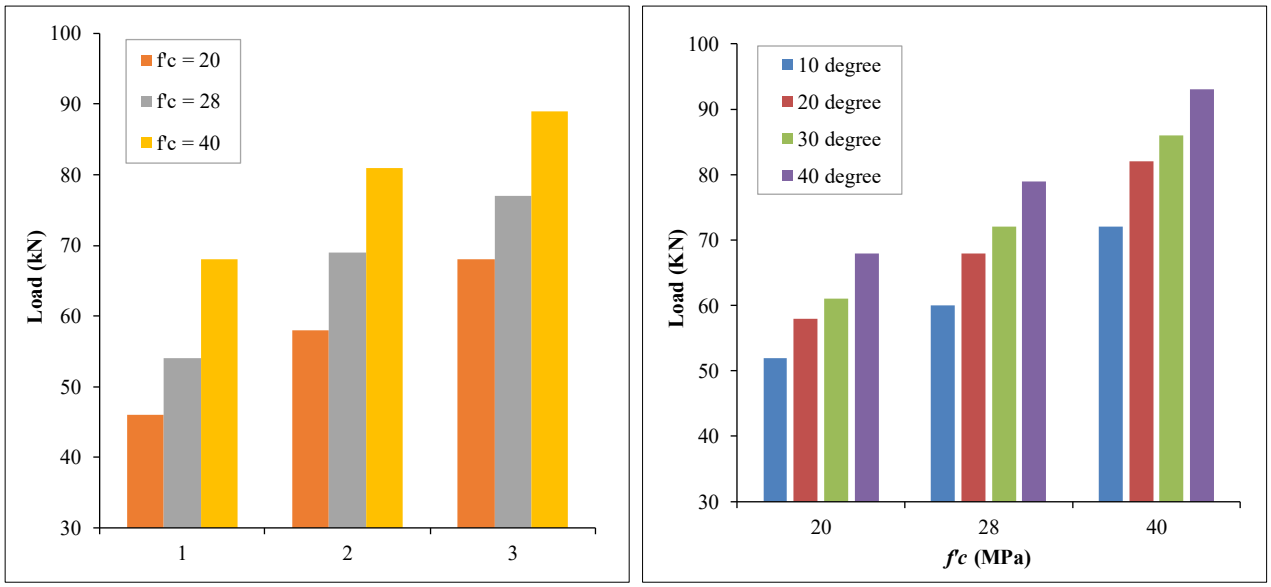

(a) *Embedded Length (cm)* (b) *f'c* (MPa)

Figure 23. Parametric comparison of ultimate load versus (a) embedded length for different *f'c* values, and (b) concrete compressive strength for varying dilation angles

At lower dilation angles, the initial load transfer is primarily governed by the existing chemical adhesion and the mechanical interlock of the rebar ribs. As the dilation angle increases toward 20°, the improved frictional resistance significantly enhances the load transfer efficiency. However, the relatively smaller gains observed between 20° and 30° indicate a phase where material nonlinearity and localized concrete softening may temporarily offset the benefits of increased dilation. Beyond the 30° threshold, the confinement effects become dominant; the high dilation induces significant radial pressure, effectively "locking" the reinforcement in place and allowing for a much larger mobilization of the concrete's compressive strength. These findings indicate that bond performance is highly sensitive to the dilation parameters of the concrete mix, highlighting the need for precise calibration in Finite Element models to accurately predict the ultimate safety limits of structural connections.

These findings align with experimental observations of bond-slip behavior in high-performance concrete matrices [65], confirming that the concrete matrix density and frictional interface are primary drivers of capacity. Furthermore, as demonstrated in recent nonlinear FEA studies, the precise calibration of confinement-related parameters—such as stirrup or volumetric restraint—is essential for capturing these non-linear transitions and ensuring the model accurately reflects real-world structural safety [66]. The underlying mechanics of this stress distribution and the potential for transition into brittle failure modes continue to be a focus of analytical and numerical investigations [67].

5. Failure Mode Analysis and Discussion

The parametric investigation of steel reinforcement embedded in concrete cylinders under push-in loading identified two distinct failure regimes, primarily governed by the anchorage length and the resulting internal stress state.

5.1. Brittle Splitting Failure in High Embedment Lengths

In specimens characterized by a high rebar embedment length (L = 9 cm), the Finite Element Analysis (FEA) captured a predominant splitting failure mode, as illustrated in Figure 24. In this configuration, the tensile damage is not localized; rather, it is extensive and distributed, with cracks propagating radially outward from the bar interface toward the concrete surface. This behavior occurs because the increased embedment length allows for the accumulation of significant hoop stresses. When these stresses exceed the concrete's tensile capacity before substantial slip can occur, the specimen fails suddenly. This brittle failure suggests that while longer embedment increases total load capacity, it may reduce the overall ductility of the connection by triggering a catastrophic breach of the concrete cover. This transition to splitting is effectively a result of the loss of effective lateral confinement; as the stress accumulation exceeds the concrete's tensile capacity, the boundary conditions at the loaded end can no longer contain the radial expansion of the concrete, leading to the observed brittle fracture [64].

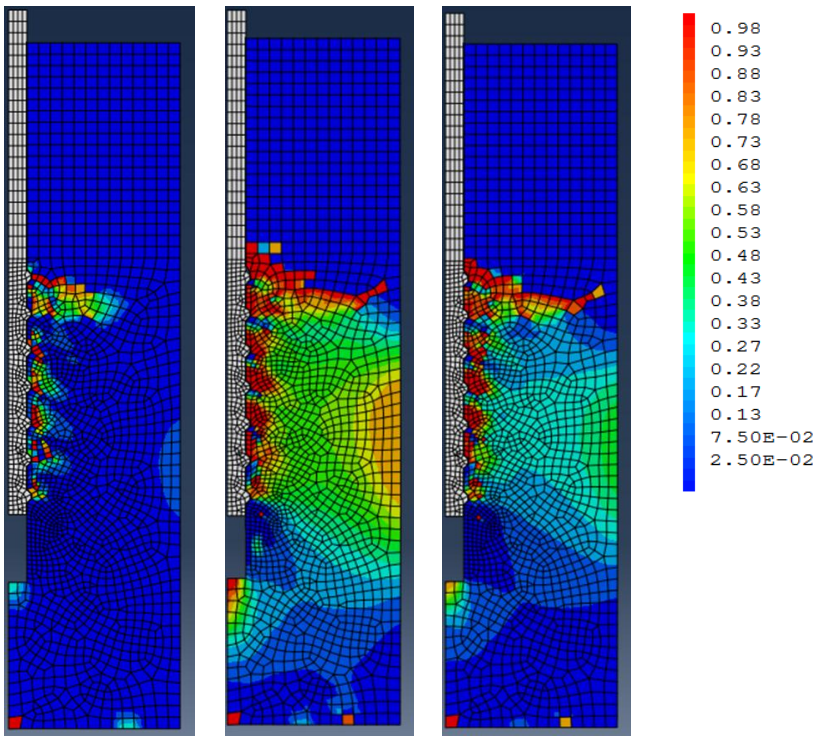

Figure 24. Predicted splitting failure mode and extensive tensile damage distribution for high rebar embedment length (L = 9 cm)

5.2. Ductile Interfacial Cracking in Low Embedment Lengths

Conversely, specimens with lower rebar embedment lengths exhibited a more stable and controlled failure mechanism, as shown in Figure 25. The FEA results indicate that tensile damage remains strictly confined within the immediate bond zone surrounding the rebar ribs. These fissures follow the geometry of the ribs, suggesting that the primary resistance is provided by the mechanical interlock and the subsequent crushing of the concrete keys. The damage pattern indicates a progressive loss of interface stiffness, leading to a controlled slip of the reinforcement rather than a sudden fracture. This ductile response is highly desirable in structural design, as it provides a predictable redistribution of stresses before ultimate failure. In this regime, the confinement provided by the base and the limited reach of the tensile stress field ensure that the failure remains localized, allowing the interface to exhibit the stable bond-slip behavior previously characterized in numerical studies of confined RC joints [66].

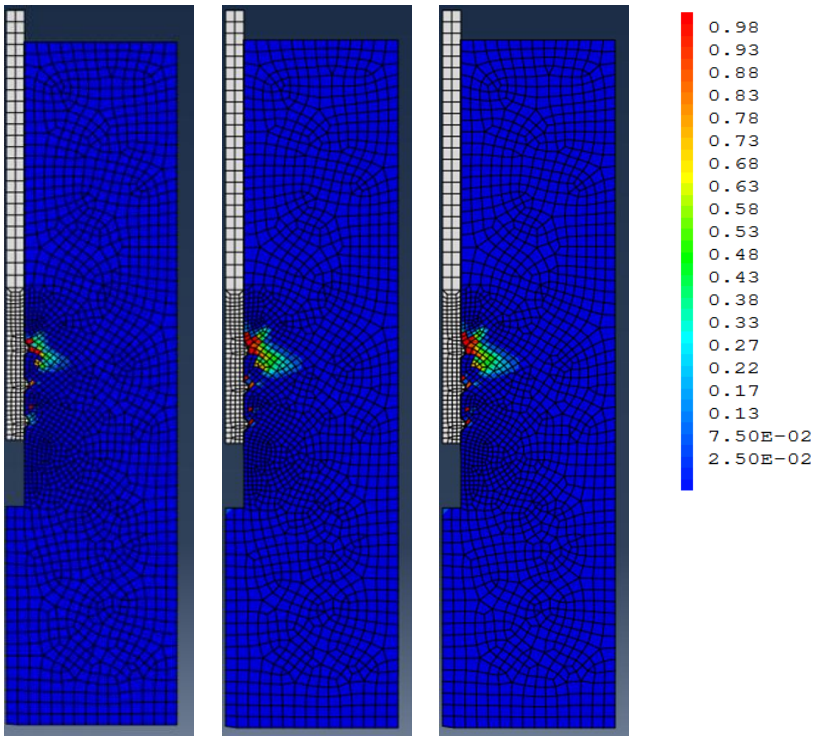

Figure 25. Predicted localized interface failure and controlled slip pattern for low rebar embedment length (L = 5 cm)

5.3. Comparative Analysis of Stress and Strain Distributions

The integration of these numerical results enhances the fundamental understanding of how concrete strength and geometric constraints dictate structural response. The transition from the localized "push-in" slip to a global "splitting" failure highlights a critical design threshold. These findings suggest that optimizing the anchorage length is not merely a matter of maximizing load, but also of ensuring that the failure mode remains ductile to prevent sudden structural collapse. Such insights are essential for advancing the performance-based design of reinforced concrete structures, particularly in seismic-prone regions where energy dissipation through controlled slip is a key safety requirement.

To further elucidate the transition in failure mechanisms between the slip mode (L = 7 cm) and the splitting mode (L = 9 cm), a detailed analysis of the internal stress and strain distributions was performed.

5.3.1. Axial Stress (σ_3) and Radial Stress (σ_1) Characteristics

As illustrated in Figure 26-a, the axial stress (σ_3) for the 7 cm anchorage is primarily concentrated at the immediate steel-concrete interface but remains relatively uniform along the bonded length. This distribution suggests a progressive debonding process where the rebar gradually displaces as bond resistance is mobilized. This behavior aligns with the findings of Li et al. (2022), who noted that optimized bond lengths enhance the uniformity of stress distribution along the interface [17].

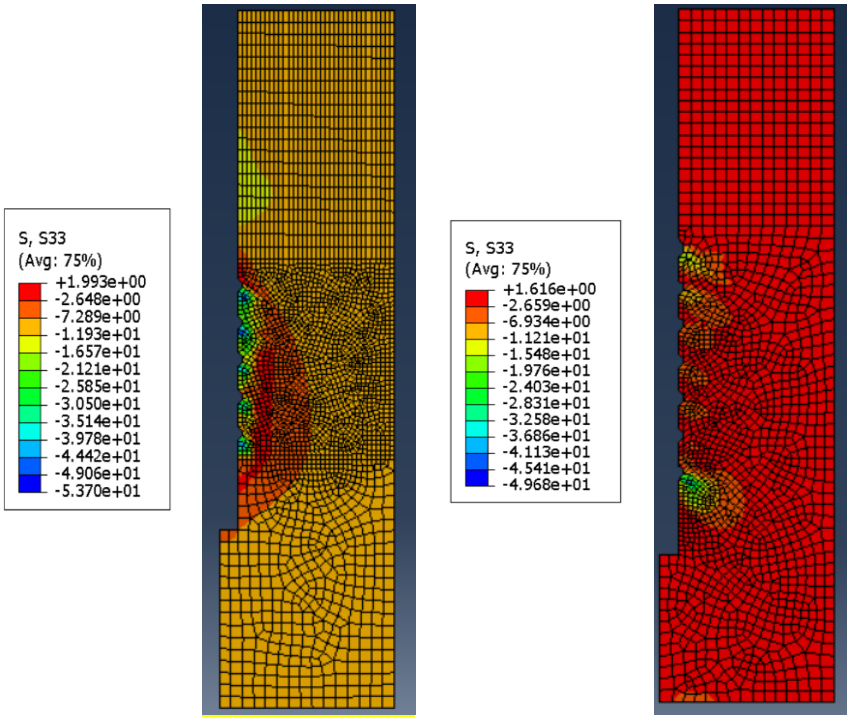

(a) (b)

Figure 26. Axial stress distribution σ_3 (MPa) a) for L=7cm, b) for L=9cm

Conversely, in the 9 cm anchorage, the concrete matrix is subjected to intense localized forces before the full bond length is efficiently utilized. As shown in Figure 26-b, the axial stress (σ_3) exhibits a significant peak near the loaded end. Radial stress (σ_1) distributions further support this observation. In the 7 cm case (Figure 27-a), $\sigma 1$ is distributed more evenly, consistent with a controlled slip failure. In the 9 cm case (Figure 27-b), however, $\sigma 1$ shows a notable concentration in the bonded region. This concentration increases the internal tensile hoop stresses in the surrounding concrete; once these stresses exceed the concrete's tensile strength, a sudden splitting failure is triggered. These stress concentrations act as initiation points for crack propagation and govern the transition from ductile to *brittle behavior*. As recently established in mechanical investigations of confined concrete, these radial stress peaks are a direct consequence of the interaction between the rebar's expansive dilation and the limited capacity of the concrete cover to provide passive confinement [64].

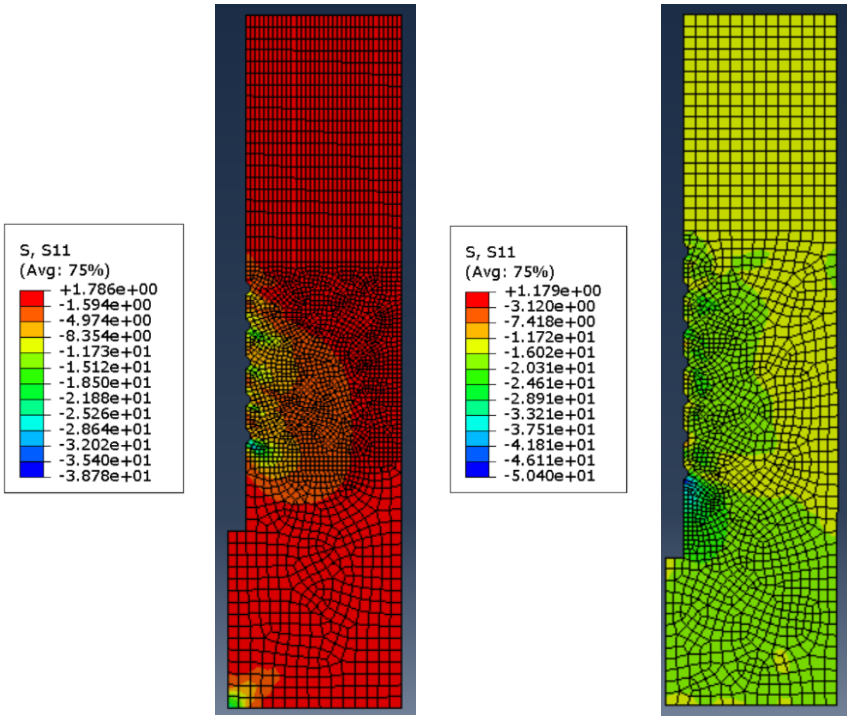

Figure 27. Radial stress distribution σ_1 (MPa) a) for L=7 cm, b) for L=9 cm

5.3.2. Principal Plastic Strain (PE_{max}) and Crack Propagation

The distribution of maximum principal plastic strain (Figures 28-a and 28-b) provides a visual representation of crack initiation. For the 7 cm anchorage, plastic strain is strictly localized along the interface, confirming a failure dominated by slip. In contrast, the 9 cm anchorage shows a much broader strain distribution that extends deep into the concrete section. This wide propagation is indicative of the splitting mode, where the concrete cylinder fails globally rather than losing bond locally.

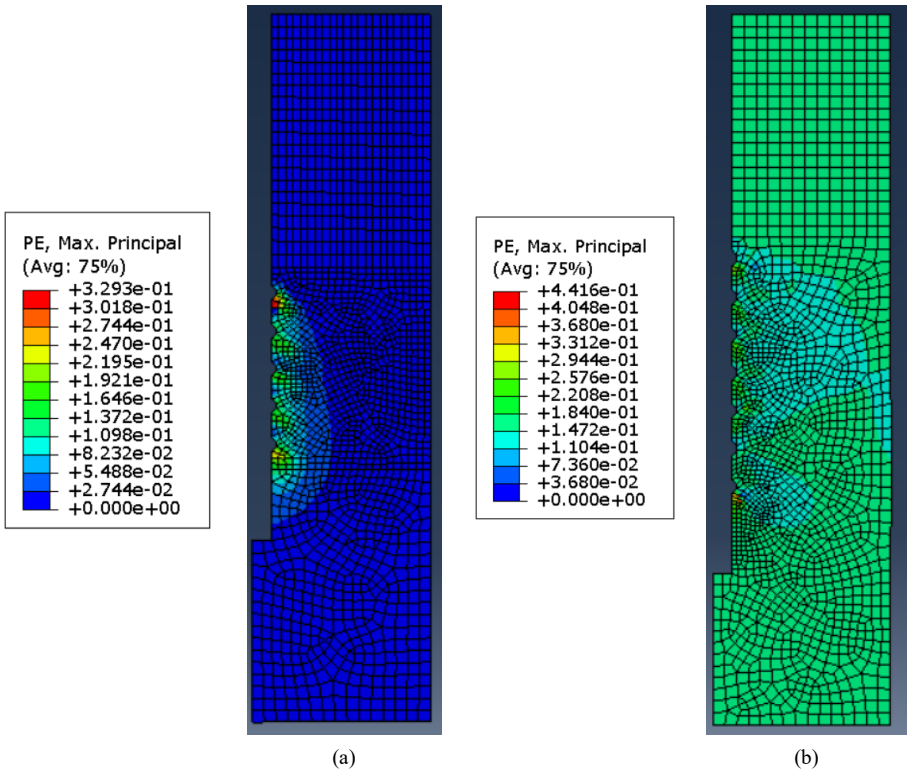

Figure 28. Strain distribution PE max a) for L=7 cm, b) for L=9 cm

The parametric study results indicate a clear trend in which shorter bond lengths significantly improve the ultimate load-bearing capacity of the steel-concrete interface. This is consistent with findings from Li et al. (2022), who also noted that reducing the bond length enhanced stress distribution along the interface [17]. However, unlike previous studies focused solely on pull-out tests, this research shows that push-in tests produce similar failure modes, confirming the utility of push-in tests as a complementary method for bond strength evaluation. These results have practical implications, particularly in the design of prestressed concrete structures where bond length and concrete strength must be optimized to enhance durability and load resistance.

This transition confirms that when the embedment length exceeds a critical threshold, the structural system undergoes a change in confinement demand, consistent with the failure regimes observed in nonlinear FEA of complex RC joints. Furthermore, the observed transition from ductile interfacial slip to brittle splitting aligns with whole-process behavior observed in other steel-concrete composite mechanisms, where localized debonding must be carefully managed to maintain global structural integrity [68]. These results have practical implications, particularly in the design of prestressed concrete structures, beam–column joints, and heavily confined elements, where bond length and concrete strength must be optimized to enhance durability and load resistance.

The findings of this study have direct implications for structural engineering practice. In particular, the identified transition between ductile slip and brittle splitting is highly relevant for the design of prestressed anchorage systems, beam–column joints in seismic regions, and heavily confined structural elements. Ensuring an optimal embedment length can enhance ductility and prevent sudden brittle failure, thereby improving structural safety and resilience. From an engineering perspective, these findings highlight the importance of optimizing embedment length and confinement conditions in reinforced concrete design. Avoiding excessive anchorage lengths can enhance ductility and reduce the risk of brittle splitting failure, particularly in seismic regions where controlled energy dissipation is essential for structural safety. Despite the strong agreement between numerical and experimental results, certain limitations should be acknowledged. The use of a 2D axisymmetric model simplifies the three-dimensional nature of the problem and may slightly overestimate confinement effects. Additionally, the assumption of a frictionless interface, while justified by the dominance of mechanical interlocking, may not fully represent all aspects of surface interaction in real structures.

5.3.3 Limitations and Model Reliability

While the experimental program utilized three specimens for the calibration of the numerical framework, it is acknowledged that this sample size is limited. Given the computational intensity of the 2D nonlinear Finite Element simulations—which incorporate detailed damage-plasticity mapping at the rib-concrete interface—the three specimens were selected to capture representative, high-fidelity bond-slip data across the targeted embedment lengths. Despite the strong agreement between numerical and experimental results, it is important to note that the 2D nonlinear framework assumes idealized bond conditions at the ribs, which may slightly simplify the stochastic nature of concrete cracking compared to full-scale experimental conditions. Furthermore, the use of a 2D axisymmetric representation, while computationally efficient for extensive parametric studies, idealizes the non-axisymmetric, three-dimensional geometry of the steel ribs. Consequently, this approach provides an averaged representation of the mechanical interlock rather than capturing the local, point-to-point stress concentrations occurring between individual ribs. However, the model maintains high predictive accuracy for macroscopic bond-slip behavior, radial confinement, and splitting failure patterns, confirming that the transition between failure regimes is reliably captured within the axisymmetric domain. Additionally, specimen variability, such as local variations in concrete heterogeneity and micro-crack distribution, may influence absolute bond capacity. To mitigate the impact of this variability, the model was calibrated using a consistent material property set derived from the experimental mean values, ensuring that the global bond-slip trends and the transition between failure regimes remain robust. Future work will aim to expand this experimental database to perform a formal sensitivity analysis on the statistical distribution of these parameters, further enhancing the predictive reliability of the FE model.

6. Conclusion

In this study, nonlinear Finite Element Analyses were conducted to rigorously investigate the failure modes, ultimate load capacities, and cracking patterns of reinforced concrete specimens subjected to push-in tests. This research focused on the mechanical behavior of the steel-concrete interface, identifying it as a critical determinant of stress transfer in structural elements. By utilizing the push-in test as a robust alternative to conventional pull-out configurations, this study successfully evaluated bond integrity under compressive stress states. Following the calibration of a 2D FEA framework against experimental benchmarks, a comprehensive parametric study of 36 models was performed, accounting for variations in embedment length, concrete compressive strength ($f'c$), and dilation angles.

The results reveal a distinct non-linear relationship between embedment length and bond efficiency. While absolute ultimate load capacity generally trends upward with length, the average bond stress exhibits a critical threshold at 7 cm. Beyond this, a reduction in average stress confirms that excessive anchorage lengths can lead to non-uniform stress

distribution and premature failure. Consistent with established mechanics, increasing *f'c* consistently enhances bond capacity, while the dilation angle emerges as a dominant factor in mobilizing passive confinement. Crucially, detailed stress and strain analyses confirmed a fundamental shift in failure mechanisms: shorter embedment lengths (5 cm and 7 cm) promote controlled, ductile interfacial slip, whereas longer embedment (9 cm) initiates brittle splitting failure characterized by radial cracking and high axial stress concentrations.

These findings demonstrate that the calibrated Concrete Damaged Plasticity (CDP) model is a highly reliable tool for simulating complex steel-concrete interactions. Furthermore, this study validates the push-in test as a superior, more representative method for evaluating bond behavior under the compressive states frequently encountered in practical structural applications. Ultimately, optimizing embedment length is not merely a matter of maximizing load; it is a necessity for ensuring ductility and structural resilience. By avoiding excessive anchorage, designers can mitigate brittle splitting risks, particularly in seismic-prone regions, thereby significantly enhancing the safety, durability, and long-term performance of reinforced concrete connections.

6.1. Future Works

Building upon these findings, future research will investigate the permeability characteristics of the steel-concrete interface, which is vital for the long-term durability of structures in aggressive environments. Additionally, transitioning to three-dimensional finite element models (3D-FEA) will allow for the simulation of more complex conditions, such as cyclic loading and environmental factors like temperature fluctuations and corrosion. These advancements will provide a more holistic understanding of interface behavior, ultimately contributing to the design of more resilient and sustainable reinforced concrete structures.

7. Nomenclature

CDP	Concrete Damaged Plasticity	*FEA*	Finite Element Analysis
f'c	Concrete compressive strength (MPa)	*L*	Embedment length (cm)
ψ	Dilation angle (°)	K_c	Yield surface shape parameter
G_f	Fracture energy (N/mm)	μ	Friction coefficient
σ_1	Radial Stress (MPa)	σ_2	Axial Stress (MPa)
PE_{max}	Maximum Principal Plastic Strain		

8. Declarations

8.1. Author Contributions

Conceptualization, G.A. and M.E.E.D.; methodology, G.A. and M.E.E.D.; software, G.A.; validation, G.A., F.A., and M.E.E.D.; formal analysis, G.A. and A.S.; investigation, G.A, R.A., and M.E.E.D.; resources, G.A, R.A., and M.E.E.D.; data curation, G.A. and M.E.E.D.; writing—original draft preparation, G.A., F.A., and M.E.E.D.; writing—review and editing, F.A., A.S., and R.A.; visualization, G.A. and F.A.; supervision, A.S. and M.E.E.D.; project administration, M.E.E.D.; funding acquisition, G.A., A.S., and R.A. All authors have read and agreed to the published version of the manuscript.

8.2. Data Availability Statement

The data presented in this study are available on request from the corresponding author.

8.3. Funding

The authors received no financial support for the research, authorship, and/or publication of this article.

8.4. Conflicts of Interest

The authors declare no conflict of interest.

9. References

[1] Reis, E. D., de Azevedo, R. C., Christoforo, A. L., Poggiali, F. S. J., & Bezerra, A. C. S. (2023). Bonding of steel bars in concrete: A systematic review of the literature. Structures, 49, 508–519. doi:10.1016/j.istruc.2023.01.141.

[2] Rabi, M., Cashell, K. A., Shamass, R., & Desnerck, P. (2020). Bond behaviour of austenitic stainless steel reinforced concrete. Engineering Structures, 221, 111027. doi:10.1016/j.engstruct.2020.111027.

[3] fib. (2012). Model Code for Concrete Structures 2010. Bulletins 65–66, International Federation for Structural Concrete (fib), Lausanne, Switzerland.

[4] Valli, A, & Kumar, R. M. S. (2023). Review on the mechanism and mitigation of cracks in concrete. Applications in Engineering Science, 16, 100154. doi:10.1016/j.apples.2023.100154.

[5] Metelli, G., & Plizzari, G. A. (2014). Influence of the relative rib area on bond behaviour. Magazine of Concrete Research, 66(6), 277–294. doi:10.1680/macr.13.00198.

[6] Eligehausen, R., Popov, E. P., & Bertero, V. V. (1983). Local bond stress-slip relationships of deformed bars under generalized excitations: experimental results and analytical model. Report No. UCB/EERC-83/23, University of California, Berkeley, United States.

[7] CEB-FIP Model Code (1990) Design Code. Thomas Telford Services Ltd., London, United Kingdom.

[8] Desnerck, P., Lees, J. M., & Morley, C. T. (2015). Bond behaviour of reinforcing bars in cracked concrete. Construction and Building Materials, 94, 126–136. doi:10.1016/j.conbuildmat.2015.06.043.

[9] Mousavi, S. S., Dehestani, M., & Mousavi, K. K. (2017). Bond strength and development length of steel bar in unconfined self-consolidating concrete. Engineering Structures, 131, 587–598. doi:10.1016/j.engstruct.2016.10.029.

[10] Metelli, G., Cairns, J., Conforti, A., & Plizzari, G. A. (2021). Local bond behavior of bundled bars: Experimental investigation. Structural Concrete, 22(4), 2322–2337. doi:10.1002/suco.202000576.

[11] Xu, C., Wang, K., & Gu, X. (2022). Study on bond behaviour of stainless steel reinforced concrete. Structures, 44, 1454–1465. doi:10.1016/j.istruc.2022.08.078.

[12] Gambarova, P. G., Plizzari, G., Rosati, G., & Russo, G. (2000). Bond mechanics including pull-out and splitting failures. Chapter 1 of Fib State-of-Art Report "Bond of Reinforcement in Concrete" (Bulletin No. 10); Fédération Internationale du Béton: Lausanne, Switzerland.

[13] ACI 408R-03. (2003Bond and Development of Straight Reinforcing Bars in Tension. American Concrete Institute (ACI), Farmington Hills, United States.

[14] Baran, E., Akis, T., & Yesilmen, S. (2012). Pull-out behavior of prestressing strands in steel fiber reinforced concrete. Construction and Building Materials, 28(1), 362–371. doi:10.1016/j.conbuildmat.2011.08.040.

[15] JGJ 387-2017. (2017). Technical specification for concrete structures prestressed with retard-bonded tendons. Ministry of Housing and Urban-Rural Development, Beijing, China.

[16] Zhang, J., Tao, X., Li, X., Zhang, Y., & Liu, Y. (2022). Analytical and experimental investigation of the bond behavior of confined high-strength recycled aggregate concrete. Construction and Building Materials, 315, 125636. doi:10.1016/j.conbuildmat.2021.125636.

[17] Li, X., Zhang, J., Liu, J., & Cao, W. (2019). Bond Behavior of Spiral Ribbed Ultra-high Strength Steel Rebar Embedded in Plain and Steel Fiber Reinforced High-Strength Concrete. KSCE Journal of Civil Engineering, 23(10), 4417–4430. doi:10.1007/s12205-019-2449-0.

[18] Zhang, X., Wang, L., Zhu, Y., Liu, J., Wang, X., Zhou, G., & Yang, J. (2026). Dynamic mechanical response and damage analysis of steel fiber-reinforced recycled aggregate concrete under repeated impact loading. Results in Engineering, 29. doi:10.1016/j.rineng.2026.109212.

[19] Wang, C., Du, Z., & Ma, Z. (2026). 4D CT–validated mesoscale finite-element modeling and coupled ITZ–fiber damage evolution in micro-steel-fiber-reinforced recycled aggregate concrete. Construction and Building Materials, 513. doi:10.1016/j.conbuildmat.2026.145443.

[20] Chao, S. H., Naaman, A. E., & Parra-Montesinos, G. J. (2006). Bond behavior of strand embedded in fiber reinforced cementitious composites. PCI Journal, 51(6), 56–71. doi:10.15554/pcij.11012006.56.71.

[21] Zhang, J., Li, X., Liu, B., Min, X., Jiang, H., & Liu, Y. (2022). Experimental investigation of the overall pull-out behavior of group anchored straight-type steel strands. Engineering Structures, 266, 114543. doi:10.1016/j.engstruct.2022.114543.

[22] Martí-Vargas, J. R., Hale, W. M., García-Taengua, E., & Serna, P. (2014). Slip distribution model along the anchorage length of prestressing strands. Engineering Structures, 59, 674–685. doi:10.1016/j.engstruct.2013.11.032.

[23] Al-Zubaidi, A. J., & Al-Saidi, A. A. H. (2025). Improving the Performance of Shallow Footing Subjected to Uplift Loading Using Structural Skirt. Civil Engineering Journal, 11(8), 3208–3222. doi:10.28991/CEJ-2025-011-08-08.

[24] Hachem, A. A. K., Khatib, J. M., & Ezzedine El Dandachy, M. (2025). Assessment of interfacial mortar-mortar bond and pure shear strength of metakaolin-based geopolymer. International Journal of Building Pathology and Adaptation, 43(4), 732–748. doi:10.1108/IJBPA-02-2024-0031.

[25] Hawa, L., El-Mir, A., Khatib, J., Nasr, D., Assaad, J., Elkordi, A., & Ezzedine El Dandachy, M. (2025). Optimization of Metakaolin-Based Geopolymer Composite for Repair Application. Journal of Composites Science, 9(10), 527. doi:10.3390/jcs9100527.

[26] Hachem, A. A. K., Barraj, F., El-Mir, A., & El Dandachy, M. E. (2025). Steel-Mortar and Flexural Mortar-Mortar Bond Strengths of Metakaolin-Based Geopolymer. Engineering Reports, 7(11). doi:10.1002/eng2.70476.

[27] Ezzedine El Dandachy, M., Hassoun, L., El-Mir, A., & Khatib, J. M. (2024). Effect of Elevated Temperatures on Compressive Strength, Ultrasonic Pulse Velocity, and Transfer Properties of Metakaolin-Based Geopolymer Mortars. Buildings, 14(7), 2126. doi:10.3390/buildings14072126.

[28] Yang, M., Xu, Q., Yuan, H., Yang, S., Jiang, Y., Zhang, C., Xu, Y., Su, C., & Zhang, Z. (2025). Bond slip behavior of light steel and foamed concrete under freeze-thaw cycles. Scientific Reports, 15(1). doi:10.1038/s41598-025-03366-0.

[29] Chen, W. F., & Han, D. J. (1988). Plasticity for Structural Engineers. Springer, New York, United States. doi:10.1007/978-1-4612-3864-5.

[30] Kachanov, L. (2013). Introduction to continuum damage mechanics. Springer Science & Business Media, Cham, Switzerland.

[31] Simo, J. C., & Ju, J. W. (1987). Strain- and stress-based continuum damage models-I. Formulation. International Journal of Solids and Structures, 23(7), 821–840. doi:10.1016/0020-7683(87)90083-7.

[32] Mazars, J., & Pijaudier-Cabot, G. (1989). Continuum Damage Theory—Application to Concrete. Journal of Engineering Mechanics, 115(2), 345–365. doi:10.1061/(asce)0733-9399(1989)115:2(345).

[33] Lemaitre, J., & Chaboche, J. L. (1994). Mechanics of solid materials. Cambridge University Press, Cambridge, United Kingdom.

[34] Hansen, N. R., & Schreyer, H. L. (1994). A thermodynamically consistent framework for theories of elastoplasticity coupled with damage. International Journal of Solids and Structures, 31(3), 359–389. doi:10.1016/0020-7683(94)90112-0.

[35] Grassl, P., & Jirásek, M. (2006). Damage-plastic model for concrete failure. International Journal of Solids and Structures, 43(22-23), 7166–7196. doi:10.1016/j.ijsolstr.2006.06.032.

[36] Chen, G. M., Teng, J. G., & Chen, J. F. (2011). Finite-Element Modeling of Intermediate Crack Debonding in FRP-Plated RC Beams. Journal of Composites for Construction, 15(3), 339–353. doi:10.1061/(asce)cc.1943-5614.0000157.

[37] Erfanian, A., & Elwi, A. E. (2019). Bond Plastic Model for Steel–Concrete Damaged Interface Element. Journal of Structural Engineering, 145(5). doi:10.1061/(asce)st.1943-541x.0002302.

[38] Ding, T., Wang, Z., Liu, H., & Xiao, J. (2023). Simulation on pull-out performance of steel bar from 3D-printed concrete. Engineering Structures, 283, 115910. doi:10.1016/j.engstruct.2023.115910.

[39] Jeon, S., Ju, M., Park, J., Choi, H., & Park, K. (2023). Prediction of concrete anchor pull-out failure using cohesive zone modeling. Construction and Building Materials, 383, 130993. doi:10.1016/j.conbuildmat.2023.130993.

[40] El Dandachy, M. E., Briffaut, M., & Dufour, F. (2024). Experimental investigation of the transfer properties of ribbed and round steel rebars concrete interfaces under shear loading and after unloading. Construction and Building Materials, 451, 138746. doi:10.1016/j.conbuildmat.2024.138746.

[41] Bouhjiti, D. E. M., Ezzedine El Dandachy, M., Dufour, F., Dal Pont, S., Briffaut, M., Baroth, J., & Masson, B. (2018). New continuous strain-based description of concrete's damage-permeability coupling. International Journal for Numerical and Analytical Methods in Geomechanics, 42(14), 1671–1697. doi:10.1002/nag.2808.

[42] El Dandachy, M. E. El, Briffaut, M., Dufour, F., & Dal Pont, S. (2025). Methods in a continuous framework to assess transfer properties of concrete structures. Results in Engineering, 26, 104736. doi:10.1016/j.rineng.2025.104736.

[43] El Dandachy, M. E. (2016). Characterization and modelling of permeability of damaged concrete: application to reinforced concrete structures. PhD Thesis, Université Grenoble Alpes, Saint-Martin-d'Hères, France.

[44] El Dandachy, M. E., AlMohamad, D., Briffaut, M., El-Mir, A., Assaad, J. J., & El-Hassan, H. (2024). Assessment of concrete-to-concrete shear bond behavior using 3-D direct shear testing. Results in Engineering, 24, 103000. doi:10.1016/j.rineng.2024.103000.

[45] Chen, F., Yu, Z., Yu, Y., & Liu, Q. (2024). Study on the bond-slip numerical simulation in the analysis of reinforced concrete wall-beam-slab joint under cyclic loading. Construction and Building Materials, 449. doi:10.1016/j.conbuildmat.2024.138266.

[46] Dassault Systèmes. (2010). Abaqus Analysis User's Manual 6.10-EF. Dassault Systèmes, Waltham, United States.

[47] Hillerborg, A. (1985). The theoretical basis of a method to determine the fracture energy GF of concrete. Materials and Structures, 18(4), 291–296. doi:10.1007/bf02472919.

[48] Murcia-Delso, J., & Benson Shing, P. (2015). Bond-Slip Model for Detailed Finite-Element Analysis of Reinforced Concrete Structures. Journal of Structural Engineering, 141(4), 4014125. doi:10.1061/(asce)st.1943-541x.0001070.

[49] Brown, C. J., Darwin, D., & McCabe, S. L. (1993). Finite element fracture analysis of steel-concrete bond. SM Report No. 36, University of Kansas Center for Research, Inc., Lawrence, United States.

[50] Lagier, F., Massicotte, B., & Charron, J.-P. (2016). 3D Nonlinear Finite-Element Modeling of Lap Splices in UHPFRC. Journal of Structural Engineering, 142(11), 4016087. doi:10.1061/(asce)st.1943-541x.0001549.

[51] Li, J. (2010). An investigation of behavior and modeling of bond for reinforced concrete. Ph.D. Thesis, University of Washington, Seattle, United States.

[52] Salem, H. M., & Maekawa, K. (2004). Pre- and Postyield Finite Element Method Simulation of Bond of Ribbed Reinforcing Bars. Journal of Structural Engineering, 130(4), 671–680. doi:10.1061/(asce)0733-9445(2004)130:4(671).

[53] Hachem, Y., Ezzedine El Dandachy, M., & Khatib, J. M. (2023). Physical, Mechanical and Transfer Properties at the Steel-Concrete Interface: A Review. Buildings, 13(4), 886. doi:10.3390/buildings13040886.

[54] Dassault Systèmes. (2014). Abaqus Analysis User's Guide, Version 6.14. Dassault Systèmes, Waltham, United States.

[55] Seok, S. (2019). ABAQUS-CDPM2: First Release. GitHub Repository, 2019. Available online: https://github.com/seungwookseok/ABAQUS-version-CDPM2 (accessed on May 2026).

[56] Courtney, T. H. (2005). Mechanical behavior of materials. Waveland Press, Long Grove, United States.

[57] Hibbeler, R. C. (2013). Statics and mechanics of materials. Oxford University Press, Oxford, United Kingdom.

[58] Callister Jr, W. D., & Rethwisch, D. G. (2020). Materials science and engineering: an introduction. John Wiley & Sons, Hoboken, United States.

[59] Genikomsou, A. S., & Polak, M. A. (2015). Finite element analysis of punching shear of concrete slabs using damaged plasticity model in ABAQUS. Engineering Structures, 98, 38–48. doi:10.1016/j.engstruct.2015.04.016.

[60] Huang, Y., Yang, Z., Ren, W., Liu, G., & Zhang, C. (2015). 3D meso-scale fracture modelling and validation of concrete based on in-situ X-ray Computed Tomography images using damage plasticity model. International Journal of Solids and Structures, 67-68, 340–352. doi:10.1016/j.ijsolstr.2015.05.002.

[61] Marium Varghese, S., Kamath, K., & Rasia Salim, S. (2023). Effect of concrete strength and tensile steel reinforcement on RC beams externally bonded with fiber reinforced polymer composites: A finite element study. Materials Today: Proceedings. doi:10.1016/j.matpr.2023.03.650.

[62] Seok, S., Haikal, G., Ramirez, J. A., Lowes, L. N., & Lim, J. (2020). Finite element simulation of bond-zone behavior of pullout test of reinforcement embedded in concrete using concrete damage-plasticity model 2 (CDPM2). Engineering Structures, 221, 110984. doi:10.1016/j.engstruct.2020.110984.

[63] Nasiri, H., Pourbaba, M., & Lotfollahi Yaghin, M. A. (2025). Numerical study on the flexural and shear behavior of steel fiber and high-strength steel combination in ultra-high-performance fiber-reinforced concrete beams under cyclic loading. Structural Concrete, 26(3), 3663–3677. doi:10.1002/suco.202300760.

[64] Khan, M. M., & Iqbal, M. A. (2024). Impact of End Friction and Lateral Inertia Confinement on the Dynamic Compressive Performance of Standard and High-Strength Concrete. Journal of Failure Analysis and Prevention, 24(2), 936–954. doi:10.1007/s11668-024-01897-8.

[65] Huang, Z., Huang, X., Li, W., Chen, C., Li, Y., Lin, Z., & Liao, W. I. (2021). Bond-slip behaviour of H-shaped steel embedded in UHPFRC. Steel and Composite Structures, 38(5), 563–582. doi:10.12989/scs.2021.38.5.000.

[66] Amirkhani, S., & Lezgy-Nazargah, M. (2022). Nonlinear finite element analysis of reinforced concrete columns: Evaluation of different modeling approaches for considering stirrup confinement effects. Structural Concrete, 23(5), 2820–2836. doi:10.1002/suco.202100532.

[67] Vořechovská, D., & Vořechovský, M. (2014). Analytical and Numerical Approaches to Modelling of Reinforcement Corrosion in Concrete. Transactions of the VŠB – Technical University of Ostrava, Civil Engineering Series, 14(1), 20–30. doi:10.2478/tvsb-2014-0003.

[68] Zhuang, L. D., Chen, H. B., Ma, Y., & Ding, R. (2021). Research on Whole-Process Tensile Behavior of Headed Studs in Steel–Concrete Composite Structures. International Journal of Concrete Structures and Materials, 15(1), 24. doi:10.1186/s40069-021-00464-x.

[69] Bazant, Z. P., & Oh, B. H. (1977). General Information. Matériaux et Constructions, 10(2), 121–122. doi:10.1007/bf02474860.

[70] Bažant, Z. P. (2001). Concrete fracture models: Testing and practice. Engineering Fracture Mechanics, 69(2), 165–205. doi:10.1016/S0013-7944(01)00084-4.

[71] Martin, J., Stanton, J., Mitra, N., & Lowes, L. N. (2007). Experimental testing to determine concrete fracture energy using simple laboratory test setup. ACI Materials Journal, 104(6), 575–584. doi:10.14359/18961.

Appendix I: CDP Model

In order to lessen the impact of mesh size sensitivity on the analytical result, the material in tension was considered by designating Gf as a material characteristic. Gf for each test specimen was determined using the empirical formula below, which was proposed by Bažant & Oh [69] and Bažant [70], and further validated by Martin et al. [71], as it was not available from the relevant literature or reports.

Rather than a stress-strain relationship, the brittle behavior of the concrete is frequently characterized by a stress-crack displacement had response (Figure A1). There are three ways to define the stress-crack displacement relationship: linear, bilinear, or exponential tension softening response. The maximum tensile strength, f_t, and the concrete's fracture energy, Gf, which is represented by the area under the tensile stress-crack displacement curve, were computed using the bilinear stiffening response employed in this investigation. The fracture energy Gf can be derived and is dependent on the aggregate size and quality of the concrete. Model Code 90 for CEB-FIP [7].

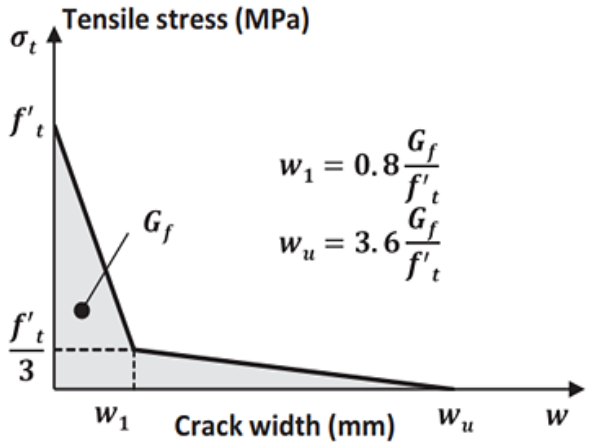

Figure A1. Uniaxial tensile stress-crack width relationship for concrete

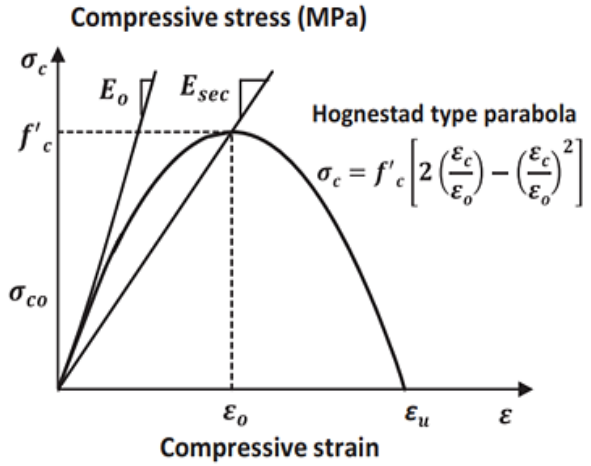

Figure A2. Uniaxial compressive stress-stain relationship for concrete

The Hognestad parabola was used to model concrete under compression (Figure A2). Three domains can be distinguished in the expected behavior of the concrete's stress-strain relation under uniaxial compressive force. The first one has the initial modulus of elasticity and represents the linear-elastic branch. $E_o = 5500\sqrt{f'c}$. At the stress level of rco that was measured here, the linear branch ends here was taken as: $\sigma_{co} = 0.4f'c$. The arising branch of the uniaxial stress-strain curve for compression loading to the peak load at the appropriate strain level is described in the second section., $e_o = 2f'_c / E_{sec}$. The secant modulus of elasticity was defined as: $E_{sec} = 5500\sqrt{f'c}$. The post-peak branch is shown as the third segment of the curve, which occurs after the peak stress and continues until the ultimate strain, or ε_u. Figures A3 and A4, respectively, show how damage was added to the CDP model in tension and compression. It was believed that both tension and compression damage to concrete would occur in the softening range. Damage was presented in compression when the peak load, or e_o, was reached.

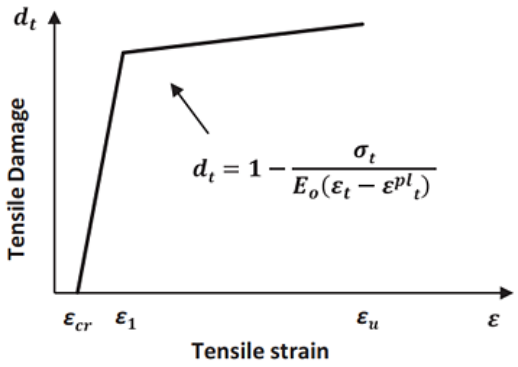

Figure A3. Tensile damage parameter-strain relationship for concrete

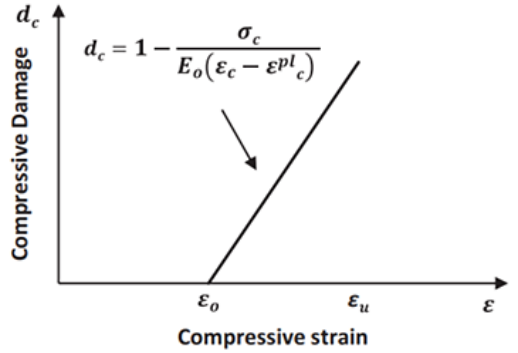

Figure A4. Compressive damage parameter-strain relationship for concrete simplified in linear form